



Nonlinear dynamics near a double Hopf bifurcation for a ship model with time-delay control

Junaidvali Shaik · Thomas K. Uchida  ·
C. P. Vyasarayani

Received: 3 April 2023 / Accepted: 27 September 2023 / Published online: 30 October 2023
© The Author(s), under exclusive licence to Springer Nature B.V. 2023

Abstract A double Hopf bifurcation analysis is performed for the rolling of a low-freeboard ship model controlled with an active U-tube anti-roll tank (ART). We consider a single-degree-of-freedom system with nonlinear damping and restoring functions. The ART is modeled as a proportional-gain controller. A constant delay term is included in the controller since a finite amount of time is required to pump the fluid inside the ART from one container to the other. We perform a linear stability analysis to determine the critical control gain and delay corresponding to the double Hopf bifurcation point. We confirm the existence of the double Hopf bifurcation by finding slopes and roots of the characteristic equation of the linearized delay differential equation with the critical parameters. We use the method of multiple scales to obtain slow-flow equations at the double Hopf bifurcation, which are then used to identify six qualitatively distinct sets of fixed points. Our analysis reveals that one of these regions has a stable zero equilibrium, another has a stable limit

cycle with amplitude smaller than the capsizing angle, and the remaining regions have no safe fixed points. These qualitative observations are validated numerically. Study of the control of ship roll motion is important to avoid dynamic instability and capsizing.

Keywords Anti-roll tank · Delay differential equation · Double Hopf bifurcation · Method of multiple scales · Ship roll dynamics

1 Introduction

Ships navigating rough seas experience several types of wave-induced excitations, which can lead to dynamic instabilities and high-amplitude rolling. The roll motion of a ship is less damped than the pitch and yaw motions [1]; in extreme cases, roll excitation can result in capsizing. Furthermore, rolling can cause seasickness, impede crew performance, and damage equipment on naval vessels. It is critical to study and understand the dynamics, stability, and control of ship roll motion to mitigate these adverse effects.

Instabilities in a ship's roll motion can be induced by two mechanisms: direct excitation and parametric excitation. Direct excitation occurs when waves collide with the port side or starboard side of a ship and can be caused by both beam waves (waves that are approximately perpendicular to the ship's heading direction) and oblique waves. If the frequency of such waves coincides with the ship's roll natural frequency, direct reso-

J. Shaik · C. P. Vyasarayani
Department of Mechanical and Aerospace Engineering, Indian
Institute of Technology Hyderabad, Sangareddy, Telangana
502285, India
e-mail: me18resch01001@iith.ac.in

C. P. Vyasarayani
e-mail: vcprakash@mae.iith.ac.in

T. K. Uchida (✉)
Department of Mechanical Engineering, University of Ottawa,
161 Louis-Pasteur, Ottawa, Ontario K1N 6N5, Canada
e-mail: tuchida@uottawa.ca

nance will occur, leading to high-amplitude rolling. To minimize direct excitation in a beam sea, ships are typically navigated perpendicular to waves, thereby resulting in a head sea or following sea. However, this strategy leads to excitation of the ship's pitch motion, which may induce parametric excitation.

Parametric excitation of the roll motion can arise from the inherent coupling between a ship's pitch and roll dynamics, from the shape of the hull, due to the ratio of the pitch and roll frequencies, and when the ship encounters a head sea or following sea whose wavelength is similar to the length of the ship [2]. Direct excitation of the pitch motion is caused by head and following waves (waves that are directed toward the bow and stern of the ship, respectively) as well as oblique waves. If the frequency of the pitch motion becomes twice the natural frequency of the roll motion, the ship experiences parametric resonance and, consequently, indirect roll excitation.

The frequency of roll excitation can be adjusted by altering the speed and heading of the ship. However, the speed and amplitude of the ocean waves cannot be controlled, and there are limitations to the rate and range of adjustments that can be made to ship speed. A more reliable strategy is to use active control methods such as bilge keels, fins, rudders, gyroscopic stabilizers, and U-tube anti-roll tanks (ARTs) [3]. ARTs have two key advantages over other control strategies. First, ARTs are not affected by the ship's forward speed, making them appropriate for use even when the vessel is moored, such as during loading and unloading operations. Second, the performance of an ART is independent of the natural frequency of either the ship or the tank.

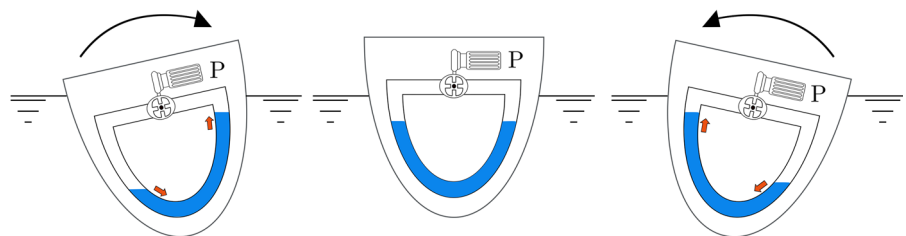
Anti-roll tanks can be either passive or actively controlled. A passive ART functions like a tuned mass-damper system. In contrast, an actively controlled ART pumps air between tanks to displace water, moving it from one tank to the other, thereby generating torques that coun-

teract the roll motion (Fig. 1). In general, time delays occur in this correction-torque control system due to the time required to displace water from one ART tank to the other, the inertia of large impeller blades and linkages in the pump, and the measurement and processing time of the roll-sensing unit. The transfer of fluid between tanks affects the restoring arm of the vessel through weight redistribution as well as the roll damping due to friction losses from fluid flow. As a result, ARTs can be modeled as proportional–derivative (PD) feedback control systems with time delay. Although an ART's hydraulics exhibit nonlinear behavior, an actively controlled ART can be operated using a simple linear proportional or PD controller [4, 5].

Here, we outline the existing literature in the area of ship dynamics. We first discuss general studies carried out in this field, then restrict our attention to studies that consider active control for ship stabilization with specific focus on studies exploring ARTs. In the mid-1980s, Nayfeh and Khdeir [6, 7] performed pioneering work in which they modeled a rolling ship as a single-degree-of-freedom nonlinear dynamical system, demonstrating the existence of chaos when the ship was subjected to beam waves. Spyrou and Thompson [8, 9], Ibrahim and Grace [10], and Neves [11] have published comprehensive reviews of the literature on ship motion dynamics.

Strategies to control the rolling of ships have been explored for many years. In 1935, Minorsky [4] analyzed the active control of ship rolling, including nonlinear damping and linear restoring moments. Minorsky proposed a control law based on the rate of rolling and its effect on roll damping, noting the importance of delay but ignoring higher-order terms in the delayed control function. In recent years, numerous studies have assessed the effects of passive and active ARTs on a ship's roll motion [12, 13] and the coupled roll, pitch, and heave motions [14, 15]. In 2001, Abdel Gawad et al. [16] studied the application of a single passive U-tube ART to control the roll motion of a ship.

Fig. 1 A ship equipped with an actively controlled anti-roll tank. The pump ("P") pumps air between tanks to displace water (block arrows) and generate corrective torques (curved arrows)



This work includes a comprehensive review of the literature on the development of ARTs. In 2009, Marzouk and Nayfeh [5] investigated an active U-tube ART controlled by a PD control law. They concluded that, compared to a passive ART, an active ART is superior in terms of roll reduction, size, weight, and responsiveness to parametric rolling. Moaleji and Greig [17] proposed an active U-tube ART that employs an adaptive inverse model as its controller.

The effect of feedback delays has been well documented and is an active topic of investigation [18]. Spyrou studied the effect of heading and yaw rate feedback delays on the performance of a course-keeping controller [19]. However, there is limited work on the effect of delays in control systems employing active U-tube ARTs to stabilize ship roll dynamics. Shaik et al. [20] analyzed the roll dynamics of a ship controlled by an active U-tube ART with delayed feedback. A detailed parametric study was performed and the controller parameters that provide maximum damping were determined. Two key findings were reported. First, derivative feedback is detrimental to the stability of ship roll motion. Hence, a proportional-feedback control law was studied, and it was shown to be capable of preventing a ship from capsizing when using the optimal gain and time delay. Second, they demonstrated the existence of Hopf bifurcation boundaries and double Hopf bifurcation points in the parameter space of time delay and proportional-control gain.

Hopf bifurcation points in ship roll models correspond to large-amplitude roll motion, which can exceed capsizing roll angles in some cases. Thus, it is crucial to understand the behavior of the system at the Hopf bifurcation points. Although Shaik et al. [20] studied single Hopf bifurcation points in detail, the system response near double Hopf bifurcation points was not explored. In the present study, we extend this work and perform a detailed double Hopf bifurcation analysis.

Double Hopf bifurcations have been investigated in the nonlinear dynamics literature in various mathematical models, using many techniques. In models comprising nonlinear ordinary differential equations (ODEs), the method of multiple scales (MMS) was employed by Yu [21]. In models governed by partial differential equations (PDEs), the MMS method has been employed [22, 23] as well as center manifold reductions and normal form theory [24, 25]. These methods have also been used successfully for systems of delay differential equations (DDEs), with appropri-

ate modifications. On this topic, we refer the reader to studies that have used center manifold reductions [26–29], normal form theory (bypassing the center manifold reductions) [30–33], and the MMS method (bypassing the center manifold reductions and normal forms) [20, 34–36].

Our formulation can be briefly summarized as follows. First, we model a low-freeboard ship undergoing rolling motion as a single-degree-of-freedom system. The system model includes nonlinear damping and restoring functions and an actively controlled ART with delayed feedback. The ART is modeled using two parameters: control function gain and time delay. After defining the system equations, we perform a stability analysis to demonstrate the existence of double Hopf bifurcation points. Finally, we investigate the system's response near the first double Hopf bifurcation point using slow-flow equations, which are obtained via the MMS method.

The remainder of the paper is organized as follows. In Sects. 2, 3, and 4, we demonstrate the existence of the first double Hopf bifurcation point using three techniques. In Sect. 2, we perform a linear stability analysis and demonstrate existence graphically. In Sects. 3 and 4, we demonstrate existence analytically and through calculation of eigenvalues, respectively. In Sect. 5, the slow-flow equations are obtained using the MMS method at the first double Hopf bifurcation point; phase portraits and a fixed-point analysis are presented. In Sect. 6, the qualitative behavior of the phase portraits is validated numerically. Finally, conclusions are presented in Sect. 7.

2 Linear stability analysis

We consider the single-degree-of-freedom system used by Shaik et al. [20] to model the rolling of a ship in a calm sea. The governing equation for the roll angle $\phi(t)$ is

$$\ddot{\phi}(t) + \omega_0^2 \phi(t) + 2\hat{\mu}_1 \dot{\phi}(t) + \hat{\mu}_3 \dot{\phi}^3(t) + \hat{\alpha}_3 \phi^3(t) + \hat{\alpha}_5 \phi^5(t) + k_p \phi(t - \tau) = 0, \quad (1)$$

where ω_0 is the roll natural frequency, $\hat{\mu}_1$ and $\hat{\mu}_3$ are the linear and cubic damping coefficients, $\hat{\alpha}_3$ and $\hat{\alpha}_5$ are coefficients of the restoring function, and $k_p \phi(t - \tau)$ is the delayed proportional control function representing the effect of an anti-roll tank. In Eq. (1), the

restoring moment is represented by an odd polynomial in ϕ as $K(\phi) = \omega_0^2\phi + \hat{\alpha}_3\phi^3 + \hat{\alpha}_5\phi^5$, with coefficients obtained from experimental data. In general, the damping moment may be represented as $D(\dot{\phi}) = 2\hat{\mu}_1\dot{\phi} + \hat{\mu}_3|\dot{\phi}|\dot{\phi}$, comprising a linear term in $\dot{\phi}$ due to viscous damping and a quadratic term due to frictional resistance and eddies around bilge keels and sharp bilge corners [37]. However, Dalzell [37] determined that the mixed linear-plus-quadratic roll damping model can be reasonably approximated by a mixed linear-plus-cubic model, namely $D(\dot{\phi}) = 2\hat{\mu}_1\dot{\phi} + \hat{\mu}_3\dot{\phi}^3$, which we have used in Eq. (1).

To investigate the linear stability of the system around the trivial fixed point $\phi = 0$, hereafter denoted $\bar{\phi}$, we substitute $\phi(t) = r(t) + \bar{\phi}$ into Eq. (1) to obtain

$$\ddot{r}(t) + \omega_0^2 r(t) + 2\hat{\mu}_1 \dot{r}(t) + \hat{\mu}_3 \dot{r}^3(t) + \hat{\alpha}_3 r^3(t) + \hat{\alpha}_5 r^5(t) + k_p r(t - \tau) = 0. \tag{2}$$

Retaining only the linear terms in $r(t)$ in Eq. (2), we obtain

$$\ddot{r}(t) + \omega_0^2 r(t) + 2\hat{\mu}_1 \dot{r}(t) + k_p r(t - \tau) = 0. \tag{3}$$

Substituting $r(t) = \beta e^{\lambda t}$ into Eq. (3) produces the following characteristic equation:

$$D(\lambda, k_p, \tau) = \lambda^2 + 2\hat{\mu}_1 \lambda + \omega_0^2 + k_p e^{-\lambda \tau} = 0, \tag{4}$$

where $\lambda, \beta \in \mathbb{C}$. Equation (4) is a transcendental equation and possesses infinitely many roots, known as characteristic exponents. To obtain the Hopf bifurcation boundary, we substitute $\lambda = j\omega_{cr}$ into Eq. (4):

$$D(\omega_{cr}, k_p, \tau) = -\omega_{cr}^2 + 2j\hat{\mu}_1\omega_{cr} + \omega_0^2 + k_p e^{-j\omega_{cr}\tau} = 0. \tag{5}$$

(Note that, if $j\omega_{cr}$ is a root of the characteristic equation, then so is its complex conjugate $-j\omega_{cr}$.) Using Euler’s formula $e^{-j\omega_{cr}\tau} = \cos(\omega_{cr}\tau) - j \sin(\omega_{cr}\tau)$, we separate $D(\omega_{cr}, k_p, \tau)$ into its real and imaginary parts to obtain the following real-valued equations:

$$R(\omega_{cr}, k_p, \tau) = k_p \cos(\omega_{cr}\tau) - \omega_{cr}^2 + \omega_0^2 = 0, \tag{6a}$$

$$C(\omega_{cr}, k_p, \tau) = 2\hat{\mu}_1\omega_{cr} - k_p \sin(\omega_{cr}\tau) = 0. \tag{6b}$$

Table 1 Parameters used in numerical analysis of low-freeboard model (obtained from Shaik et al. [20])

Parameter	Value
Coefficients of damping function	
Linear ($\hat{\mu}_1$)	0.0855 s ⁻¹
Cubic ($\hat{\mu}_3$)	0.108 s
Coefficients of restoring function	
Linear (ω_0)	5.229 s ⁻¹
Cubic ($\hat{\alpha}_3$)	-1.699119 ω_0^2 s ⁻²
Quintic ($\hat{\alpha}_5$)	0.63297 ω_0^2 s ⁻²
Critical roll angle (ϕ_{cr})	0.48 rad

We solve Eqs. (6a) and (6b) to obtain the following linear stability boundary in the space of k_p and τ :

$$k_p = \sqrt{4\hat{\mu}_1^2\omega_{cr}^2 + (\omega_{cr}^2 - \omega_0^2)^2}, \tag{7a}$$

$$\tau = \frac{2}{\omega_{cr}} \left[n\pi + \arctan\left(\frac{k_p - \omega_{cr}^2 + \omega_0^2}{2\hat{\mu}_1\omega_{cr}}\right) \right], \tag{7b}$$

$n = 0, 1, 2, \dots$

Equations (7a) and (7b) represent a family of curves called the stability lobes, where n is the lobe number.

For the numerical analysis that follows, we use the parameter values used in the low-freeboard model of Wright and Marshfield [38]. The values of the system parameters related to the damping and restoring functions are given in Table 1. The critical roll angle ϕ_{cr} given in Table 1 is defined as the roll angle associated with the maximum restoring moment $K(\phi)$ before capsizing. The critical roll angle can be obtained by plotting $K(\phi)$ vs. ϕ , as shown in Fig. 2 for the parameters given in Table 1. (This curve is also known as the GZ curve.)

The stability boundaries of the system for lobes $n = 0$ and $n = 1$ are shown in Fig. 3. Similar lobes can be evaluated for $n \geq 2$; however, the present analysis concerns the first double Hopf bifurcation point, which occurs at the intersection of the lobes corresponding to $n = 0$ and $n = 1$. Hence, we focus on only these two lobes. (Note that, to plot the stability boundary, we vary the independent parameter ω_{cr} between a very small positive number and a very large number.) Hereafter, we refer to the values of the delay and the proportional gain at the first double Hopf bifurcation point as the “critical parameters” for brevity, and denote them as

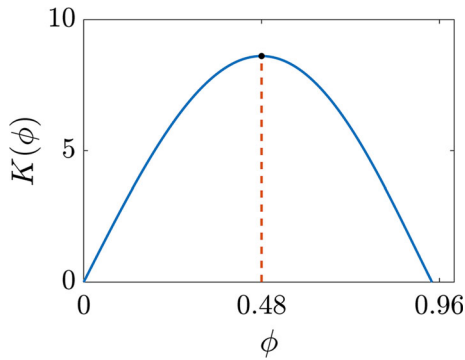


Fig. 2 The restoring function $K(\phi)$ vs. roll angle ϕ for the low-freeboard model. $K(\phi)$ reaches a maximum at the critical roll angle ϕ_{cr}

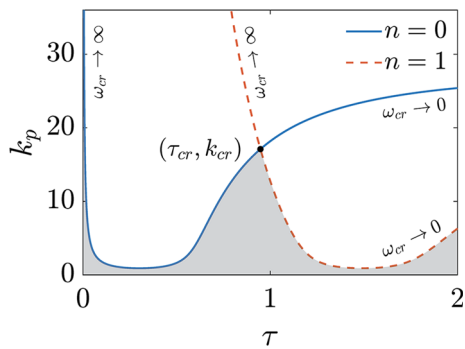


Fig. 3 Linear stability chart near the double Hopf bifurcation point in the parameter space of (τ, k_p) . The critical parameters are $(\tau_{cr}, k_{cr}) = (0.9475, 17.0998)$. The shaded region indicates stable zero equilibrium

τ_{cr} and k_{cr} , respectively. From Fig. 3, their values are $(\tau_{cr}, k_{cr}) = (0.9475, 17.0998)$,

and the corresponding frequencies are

$$\omega_1 = 3.2811 \quad \text{and} \quad \omega_2 = 6.7023, \tag{9}$$

for lobes $n = 0$ and $n = 1$, respectively.

3 Analytical demonstration of existence of double Hopf bifurcation

In this section, we demonstrate the existence of the double Hopf bifurcation point analytically by computing the crossing velocities of the eigenvalues of Eq. (3) at the critical parameters. As mentioned earlier, at the stability boundary, the eigenvalues λ cross the imaginary axis of the complex plane. Mathematically, this

means $\Re\left(\frac{\partial\lambda}{\partial k_p}\right) \neq 0$ and $\Re\left(\frac{\partial\lambda}{\partial\tau}\right) \neq 0$, where $\Re(\cdot)$ is the real part of a complex number [39,40]. We obtain the partial derivatives $\partial\lambda/\partial k_p$ and $\partial\lambda/\partial\tau$ from implicit differentiation of Eq. (4):

$$\frac{\partial\lambda}{\partial k_p} = -\frac{\partial D}{\partial k_p} \left(\frac{\partial D}{\partial\lambda}\right)^{-1} = \frac{-e^{-\lambda\tau}}{2\lambda + 2\hat{\mu}_1 - \tau k_p e^{-\lambda\tau}}, \tag{10a}$$

$$\frac{\partial\lambda}{\partial\tau} = -\frac{\partial D}{\partial\tau} \left(\frac{\partial D}{\partial\lambda}\right)^{-1} = \frac{k_p \lambda e^{-\lambda\tau}}{2\lambda + 2\hat{\mu}_1 - \tau k_p e^{-\lambda\tau}}. \tag{10b}$$

Substituting $\lambda = j\omega_i$ and $e^{-j\omega_i\tau} = \cos(\omega_i\tau) - j \sin(\omega_i\tau)$ into Eqs. (10a) and (10b), we obtain the following expressions for the real parts of the slopes:

$$\begin{aligned} \gamma_{1i} &= \Re\left(\frac{\partial\lambda}{\partial k_p}\right)\Big|_{\lambda=j\omega_i} \\ &= \left[\tau (\omega_0^2 - \omega_i^2)^2 + 4\tau\hat{\mu}_1^2 + 2\hat{\mu}_1 (\omega_0^2 + \omega_i^2) \right] / \\ &\quad \left[k_p \tau^2 \left((\omega_0^2 - \omega_i^2)^2 + 4\hat{\mu}_1^2 \right) + 4k_p \hat{\mu}_1 \tau (\omega_0^2 + \omega_i^2) + 4k_p (\hat{\mu}_1^2 + \omega_i^2) \right], \end{aligned} \tag{11a}$$

$$\begin{aligned} \gamma_{2i} &= \Re\left(\frac{\partial\lambda}{\partial\tau}\right)\Big|_{\lambda=j\omega_i} = \left[2\omega_i^2 (\omega_i^2 - \omega_0^2 + 2\hat{\mu}_1^2) \right] / \\ &\quad \left[\tau^2 (\omega_0^2 - \omega_i^2)^2 + 4\tau^2 \hat{\mu}_1^2 + 4\hat{\mu}_1 \tau (\omega_0^2 + \omega_i^2) + 4 (\hat{\mu}_1^2 + \omega_i^2) \right], \end{aligned} \tag{11b}$$

where the index $i \in \{1, 2\}$ corresponds to the critical frequencies ω_1 and ω_2 at the double Hopf bifurcation point. We define a square matrix

$$\mathbf{\Lambda} = \begin{bmatrix} \gamma_{11} & \gamma_{12} \\ \gamma_{21} & \gamma_{22} \end{bmatrix}, \tag{12}$$

whose determinant must be nonzero for the existence of a double Hopf bifurcation at the critical point [41]. Using the parameters $k_p = 17.0998$, $\tau = 0.9475$, $\omega_1 = 3.2811$, and $\omega_2 = 6.7023$, $\mathbf{\Lambda}$ at the critical point is evaluated as follows:

$$\mathbf{\Lambda} = \begin{bmatrix} 0.0521 & 0.0363 \\ -1.1557 & 3.2934 \end{bmatrix}, \tag{13}$$

and $\det(\mathbf{\Lambda}) = 0.2135$, proving the existence of the double Hopf bifurcation point.

4 Demonstration of existence of double Hopf bifurcation via eigenvalue computation

In this section, we demonstrate the occurrence of a double Hopf bifurcation point through direct computation. Specifically, we show that two pairs of purely imaginary complex-conjugate eigenvalues exist at the double Hopf bifurcation point and that the eigenvalues cross the imaginary axis upon perturbing k_p and τ around that point. Because Eq. (4) is transcendental, we use a combination of spectral Tau [42] and Newton–Raphson methods to compute its roots.

To use the spectral Tau method, we first write Eq. (3) as a pair of first-order differential equations in state variables $\mathbf{r}(t) = [r(t), \dot{r}(t)]^T$:

$$\dot{\mathbf{r}}(t) = \mathbf{B}_1 \mathbf{r}(t) + \mathbf{B}_2 \mathbf{r}(t - \tau), \tag{14a}$$

$$\mathbf{r}(t) = \boldsymbol{\gamma}(t), \quad t \in [-\tau, 0), \tag{14b}$$

where $\mathbf{B}_1 = \begin{bmatrix} 0 & 1 \\ -\omega_0^2 & -2\hat{\rho}_1 \end{bmatrix}$, $\mathbf{B}_2 = \begin{bmatrix} 0 & 0 \\ -k_p & 0 \end{bmatrix}$, and $\boldsymbol{\gamma}(t)$ is the history function. We then introduce a time shift in $\mathbf{r}(t)$:

$$\mathbf{r}(t + s) = \mathbf{y}(s, t), \quad s \in [-\tau, 0). \tag{15}$$

Due to this transformation, the initial-value problem expressed by Eq. (14) is transformed into the following boundary-value problem:

$$\frac{\partial \mathbf{y}(s, t)}{\partial t} = \frac{\partial \mathbf{y}(s, t)}{\partial s}, \tag{16a}$$

$$\left. \frac{\partial \mathbf{y}(s, t)}{\partial t} \right|_{s=0} = \mathbf{B}_1 \mathbf{y}(0, t) + \mathbf{B}_2 \mathbf{y}(-\tau, t), \tag{16b}$$

$$\mathbf{y}(s, 0) = \boldsymbol{\gamma}(s), \quad s \in [-\tau, 0). \tag{16c}$$

We assume a solution for Eq. (16a) of the following form:

$$y_i(s, t) = \sum_{j=1}^{\infty} \Psi_j(s) z_{ij}(t), \quad i = 1, 2, \tag{17}$$

where $\Psi_j(s)$ are appropriate basis functions (see Appendix A) and $z_{ij}(t)$ are time-dependent coordinates. We retain N terms in the expansion:

$$y_i(s, t) = \boldsymbol{\Psi}^T(s) \mathbf{z}_i(t), \tag{18}$$

where $\boldsymbol{\Psi}$ and \mathbf{z}_i are column vectors of dimension N . Accordingly, $\mathbf{y}(s, t)$ can be written as

$$\mathbf{y}(s, t) = \boldsymbol{\Theta}^T(s) \boldsymbol{\eta}(t), \tag{19}$$

where $\boldsymbol{\Theta} = \text{diag}(\boldsymbol{\Psi}(s), \boldsymbol{\Psi}(s)) \in \mathbb{R}^{2N \times 2}$ and $\boldsymbol{\eta} = [z_1(t), z_2(t)]^T \in \mathbb{R}^{2N \times 1}$. We substitute Eq. (19) into Eq. (16a) to obtain

$$\boldsymbol{\Theta}^T(s) \dot{\boldsymbol{\eta}}(t) = (\boldsymbol{\Theta}'(s))^T \boldsymbol{\eta}(t), \tag{20}$$

where $\dot{\boldsymbol{\eta}}(t) = \frac{d\boldsymbol{\eta}(t)}{dt}$ and $\boldsymbol{\Theta}'(s) = \frac{d\boldsymbol{\Theta}(s)}{ds}$. We pre-multiply both sides of Eq. (20) by $\boldsymbol{\Theta}(s)$ and integrate over the domain $s \in [-\tau, 0)$ to obtain the following set of ODEs:

$$\mathbf{W} \dot{\boldsymbol{\eta}}(t) = \mathbf{Q} \boldsymbol{\eta}(t), \tag{21}$$

where $\mathbf{W} = \text{diag}(\mathbf{W}^{(1)}, \mathbf{W}^{(2)})$, $\mathbf{Q} = \text{diag}(\mathbf{Q}^{(1)}, \mathbf{Q}^{(2)})$, and

$$\mathbf{W}^{(i)} = \int_{-\tau}^0 \boldsymbol{\Psi}(s) \boldsymbol{\Psi}(s)^T ds, \tag{22a}$$

$$\mathbf{Q}^{(i)} = \int_{-\tau}^0 \boldsymbol{\Psi}(s) (\boldsymbol{\Psi}'(s))^T ds, \quad i = 1, 2. \tag{22b}$$

The boundary conditions are obtained by substituting Eq. (19) into Eq. (16b):

$$\boldsymbol{\Theta}^T(0) \dot{\boldsymbol{\eta}}(t) = \mathbf{B}_1 \boldsymbol{\Theta}^T(0) \boldsymbol{\eta}(t) + \mathbf{B}_2 \boldsymbol{\Theta}^T(-\tau) \boldsymbol{\eta}(t). \tag{23}$$

Equations (21) and (23) comprise a system of $2N + 2$ linear scalar equations in $2N$ variables—an over-determined system. We remove the N th and $2N$ th equations from Eq. (21) and replace them with Eq. (23). The resulting set of equations can be written as

$$\mathbf{M} \dot{\boldsymbol{\eta}}(t) = \mathbf{K} \boldsymbol{\eta}(t). \tag{24}$$

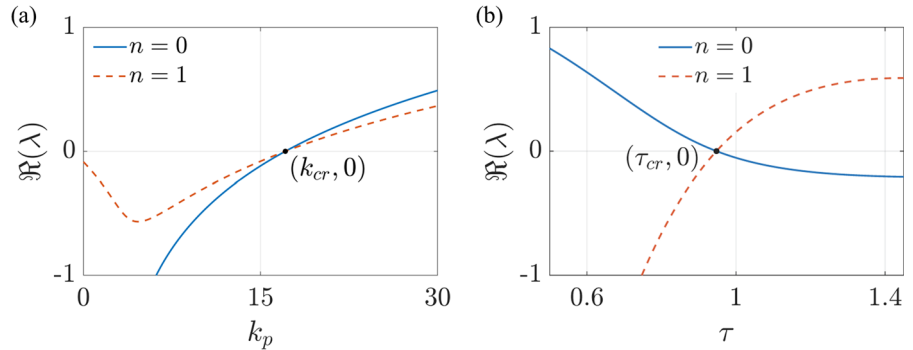
Finally, we re-write Eq. (24) as

$$\dot{\boldsymbol{\eta}}(t) = \mathbf{G} \boldsymbol{\eta}(t), \tag{25}$$

where $\mathbf{G} = \mathbf{M}^{-1} \mathbf{K}$. Equation (25) is a system of linear first-order differential equations; hence, the rightmost eigenvalues of \mathbf{G} determine the stability of the zero equilibrium.

Figure 4 illustrates the evolution of the real part of the rightmost eigenvalues of \mathbf{G} as k_p varies with $\tau = \tau_{cr}$ fixed, and as τ varies with $k_p = k_{cr}$ fixed. We note two observations in Fig. 4a, for both $n = 0$ and $n = 1$: (1) at the critical point $(\tau, k_p) = (0.9475, 17.0998)$, the real part of λ is zero; and (2) as k_p varies with τ held fixed, the real part of λ changes sign. Analogous observations are noted in Fig. 4b. We conclude that the critical point discussed above is a double Hopf bifurcation point.

Fig. 4 Evolution of the real part of the rightmost characteristic roots near the critical point **a** with k_p where $\tau = \tau_{cr}$ is fixed, and **b** with τ where $k_p = k_{cr}$ is fixed, for $N = 20$



To verify the correctness of our approach, we compute the slopes of the curves plotted in Fig. 4 and arrange them in the following matrix:

$$\Lambda_1 = \begin{bmatrix} 0.0524 & 0.0365 \\ -1.1535 & 3.2872 \end{bmatrix}. \tag{26}$$

We see that $\Lambda_1 \approx \Lambda$ (Eq. (13)), confirming agreement with our previous analysis.

5 Slow-flow equations at the double Hopf bifurcation point

Slow-flow equations are used to approximate systems of ordinary or delay differential equations governing mechanical systems. In general, slow-flow equations are first-order ODEs, thus determining fixed points and performing stability analyses are simplified. In this section, we derive slow-flow equations for Eq. (2) at the double Hopf bifurcation point. Usually, slow-flow equations at a Hopf bifurcation point are obtained using the method of center manifold reduction [43,44] or the method of multiple scales (MMS) [35,36]. For the analysis that follows, we use MMS.

We begin by scaling the time in Eq. (2) as $\bar{t} = (1 + \epsilon\Delta)t$ to introduce a perturbation in the delay parameter τ near the critical point [36], whereupon we obtain the following:

$$\begin{aligned} \ddot{r}(\bar{t}) + \frac{\omega_0^2}{(1 + \epsilon\Delta)^2} r(\bar{t}) + \frac{2\hat{\mu}_1}{1 + \epsilon\Delta} \dot{r}(\bar{t}) \\ + (1 + \epsilon\Delta) \hat{\mu}_3 \dot{r}^3(\bar{t}) + \frac{1}{(1 + \epsilon\Delta)^2} \\ \left(\hat{\alpha}_3 r^3(\bar{t}) + \hat{\alpha}_5 r^5(\bar{t}) + k_p r(\bar{t} - \bar{\tau}) \right) = 0, \end{aligned} \tag{27}$$

where derivatives are taken with respect to \bar{t} . A delay of τ_{cr} in the \bar{t} time scale corresponds to a delay of

$\frac{\tau_{cr}}{1 + \epsilon\Delta}$ in the original time t . Hence, as $\epsilon\Delta$ increases, the delay in the original time scale decreases. For notational convenience, we drop the bars over t and τ , and use ϵ as a book-keeping parameter. Substituting $k_p = k_{cr} + \epsilon\delta$, $\hat{\mu}_3 = \epsilon\mu_3$, $\hat{\alpha}_3 = \epsilon\alpha_3$, $\hat{\alpha}_5 = \epsilon\alpha_5$, $(1 + \epsilon\Delta)^{-1} = 1 - \epsilon\Delta + \mathcal{O}((\epsilon\Delta)^2)$, and $(1 + \epsilon\Delta)^{-2} = 1 - 2\epsilon\Delta + \mathcal{O}((\epsilon\Delta)^2)$ into Eq. (27), we obtain the following:

$$\begin{aligned} \ddot{r}(t) + \omega_0^2 r(t) + 2\hat{\mu}_1 \dot{r}(t) + k_{cr} r(t - \tau_{cr}) \\ + \epsilon \left[\mu_3 \dot{r}^3(t) + \alpha_3 r^3(t) + \alpha_5 r^5(t) + \delta r(t - \tau_{cr}) \right. \\ \left. - 2\omega_0^2 \Delta r(t) - 2\hat{\mu}_1 \Delta \dot{r}(t) - 2\Delta k_{cr} r(t - \tau_{cr}) \right] \\ + \mathcal{O}(\epsilon^2) = 0. \end{aligned} \tag{28}$$

For $\epsilon = 0$, Eq. (28) becomes a linear DDE with damping; hence, Eq. (28) represents the perturbation of Eq. (27).

We assume

$$r(t) = r_0(T_0, T_1) + \epsilon r_1(T_0, T_1), \tag{29}$$

where $T_0 = t$ and $T_1 = \epsilon t$. Substituting Eq. (29) into Eq. (28) and equating the coefficients of the first two powers of ϵ to zero, we obtain the following:

$$\begin{aligned} \mathcal{O}(\epsilon^0): \\ D_0^2 r_0(T_0, T_1) + 2\hat{\mu}_1 D_0 r_0(T_0, T_1) + \omega_0^2 r_0(T_0, T_1) \\ + k_{cr} r_0(T_0 - \tau_{cr}, T_1) = 0, \end{aligned} \tag{30a}$$

$$\begin{aligned} \mathcal{O}(\epsilon^1): \\ D_0^2 r_1(T_0, T_1) + 2\hat{\mu}_1 D_0 r_1(T_0, T_1) + \omega_0^2 r_1(T_0, T_1) \\ + k_{cr} r_1(T_0 - \tau_{cr}, T_1) + 2D_{0,1}^2 r_0(T_0, T_1) \\ - 2\omega_0^2 \Delta r_0(T_0, T_1) - 2\hat{\mu}_1 \Delta D_0 r_0(T_0, T_1) \\ - 2\Delta k_{cr} r_0(T_0 - \tau_{cr}, T_1) + 2\hat{\mu}_1 D_1 r_0(T_0, T_1) \end{aligned}$$

$$\begin{aligned}
 & + \mu_3 (D_0 r_0(T_0, T_1))^3 + \alpha_3 r_0^3(T_0, T_1) + \alpha_5 r_0^5(T_0, T_1) \\
 & + \delta r_0(T_0 - \tau_{cr}, T_1) - \Delta D_0 r_0(T_0 - \tau_{cr}, T_1) \\
 & - k_{cr} \tau_{cr} D_1 r_0(T_0 - \tau_{cr}, T_1) = 0, \tag{30b}
 \end{aligned}$$

where $D_i = \frac{\partial}{\partial T_i}$ and $D_{i,j} = \frac{\partial^2}{\partial T_i \partial T_j}$. Because we are considering a double Hopf bifurcation, we assume a solution to Eq. (30a) of the form

$$\begin{aligned}
 r_0(t) = & A_1(T_1) \sin(\omega_1 T_0) + A_2(T_1) \cos(\omega_1 T_0) \\
 & + A_3(T_1) \sin(\omega_2 T_0) + A_4(T_1) \cos(\omega_2 T_0). \tag{31}
 \end{aligned}$$

Substituting Eq. (31) into Eq. (30b) yields

$$\begin{aligned}
 & D_0^2 r_1(T_0, T_1) + 2\hat{\mu}_1 D_0 r_1(T_0, T_1) + \omega_0^2 r_1(T_0, T_1) \\
 & + k_{cr} r_1(T_0 - \tau_{cr}, T_1) + P_1 \cos(\omega_1 T_0) + P_2 \sin(\omega_1 T_0) \\
 & + P_3 \cos(\omega_2 T_0) + P_4 \sin(\omega_2 T_0) + P_5 \cos(3\omega_1 T_0) \\
 & + P_6 \sin(3\omega_1 T_0) + P_7 \cos(3\omega_2 T_0) + P_8 \sin(3\omega_2 T_0) \\
 & + P_9 \cos(5\omega_1 T_0) + P_{10} \sin(5\omega_1 T_0) + P_{11} \cos(5\omega_2 T_0) \\
 & + P_{12} \sin(5\omega_2 T_0) + P_{13} \cos((\omega_1 - 2\omega_2)T_0) \\
 & + P_{14} \sin((\omega_1 - 2\omega_2)T_0) + P_{15} \cos((2\omega_1 - \omega_2)T_0) \\
 & + P_{16} \sin((2\omega_1 - \omega_2)T_0) + P_{17} \cos((\omega_1 + 2\omega_2)T_0) \\
 & + P_{18} \sin((\omega_1 + 2\omega_2)T_0) + P_{19} \cos((2\omega_1 + \omega_2)T_0) \\
 & + P_{20} \sin((2\omega_1 + \omega_2)T_0) + P_{21} \cos((4\omega_1 + \omega_2)T_0) \\
 & + P_{22} \sin((4\omega_1 + \omega_2)T_0) + P_{23} \cos((\omega_1 + 4\omega_2)T_0) \\
 & + P_{24} \sin((\omega_1 + 4\omega_2)T_0) + P_{25} \cos((2\omega_1 + 3\omega_2)T_0) \\
 & + P_{26} \sin((2\omega_1 + 3\omega_2)T_0) + P_{27} \cos((3\omega_1 + 2\omega_2)T_0) \\
 & + P_{28} \sin((3\omega_1 + 2\omega_2)T_0) + P_{29} \cos((3\omega_1 - 2\omega_2)T_0) \\
 & + P_{30} \sin((3\omega_1 - 2\omega_2)T_0) + P_{31} \cos((2\omega_1 - 3\omega_2)T_0) \\
 & + P_{32} \sin((2\omega_1 - 3\omega_2)T_0) + P_{33} \cos((4\omega_1 - \omega_2)T_0) \\
 & + P_{34} \sin((4\omega_1 - \omega_2)T_0) + P_{35} \cos((\omega_1 - 4\omega_2)T_0) \\
 & + P_{36} \sin((\omega_1 - 4\omega_2)T_0) = 0. \tag{32}
 \end{aligned}$$

The coefficients $P_1, P_2, P_3,$ and P_4 in Eq. (32) correspond to secular terms and therefore, can be equated to zero, yielding $\frac{dA_i(T_1)}{dT_1}$ for $i \in \{1, 2, 3, 4\}$. Moreover, for each of the cases $\omega_1 = 3\omega_2, \omega_2 = 3\omega_1, \omega_1 = 5\omega_2,$ and $\omega_2 = 5\omega_1,$ additional secular terms arise, and must duly considered. For instance, when $\omega_1 = 3\omega_2,$ the coefficients P_{13} and P_{14} are added to P_3 and $P_4,$ respectively. However, for the current analysis, $\omega_2 = 2.0427\omega_1$ (see Eq. (9)), hence additional secular terms do not arise in our case. The coefficients P_i have lengthy expressions; thus, we list only the pertinent coefficients $P_1, P_2, P_3,$ and P_4 in Appendix B.

We equate the coefficients $P_1, P_2, P_3,$ and P_4 to zero and solve the resulting equations to obtain the derivatives $\frac{dA_i(T_1)}{dT_1}$ for $i \in \{1, 2, 3, 4\}$. These derivatives are then used to calculate

$$\frac{dA_i}{dT_0} = \epsilon \frac{dA_i}{dT_1} + \mathcal{O}(\epsilon^2), \quad i \in \{1, 2, 3, 4\}. \tag{33}$$

Next, we introduce polar coordinates and represent A_i as follows:

$$A_1(T_0) = R_1(T_0) \cos(\phi_1(T_0)), \tag{34a}$$

$$A_2(T_0) = R_1(T_0) \sin(\phi_1(T_0)), \tag{34b}$$

$$A_3(T_0) = R_2(T_0) \cos(\phi_2(T_0)), \tag{34c}$$

$$A_4(T_0) = R_2(T_0) \sin(\phi_2(T_0)). \tag{34d}$$

Substituting Eqs. (34) into Eq. (31), we obtain

$$\begin{aligned}
 r_0(T_0) = & R_1(T_0) \sin(\omega_1 T_0 + \phi_1(T_0)) \\
 & + R_2(T_0) \sin(\omega_2 T_0 + \phi_2(T_0)). \tag{35}
 \end{aligned}$$

Equations (34) are then substituted into Eqs. (33), and the resulting equations are solved for $\frac{dR_1}{dT_0}, \frac{dR_2}{dT_0}, \frac{d\phi_1}{dT_0},$ and $\frac{d\phi_2}{dT_0}$ to obtain the following slow-flow equations:

$$\begin{aligned}
 \frac{dR_1}{dT_0} = & \frac{R_1}{H_1} (N_{11} R_1^4 + N_{12} R_2^4 + N_{13} R_1^2 R_2^2 \\
 & + N_{14} R_1^2 + N_{15} R_2^2 + N_{16}(\epsilon \Delta) + N_{17}(\epsilon \delta)), \tag{36a}
 \end{aligned}$$

$$\begin{aligned}
 \frac{dR_2}{dT_0} = & \frac{R_2}{H_2} (N_{21} R_1^4 + N_{22} R_2^4 + N_{23} R_1^2 R_2^2 \\
 & + N_{24} R_1^2 + N_{25} R_2^2 + N_{26}(\epsilon \Delta) + N_{27}(\epsilon \delta)), \tag{36b}
 \end{aligned}$$

$$\begin{aligned}
 \frac{d\phi_1}{dT_0} = & \frac{1}{H_1} (N_{31} R_1^4 + N_{32} R_2^4 + N_{33} R_1^2 R_2^2 \\
 & + N_{34} R_1^2 + N_{35} R_2^2 + N_{36}(\epsilon \Delta) + N_{37}(\epsilon \delta)), \tag{36c}
 \end{aligned}$$

$$\begin{aligned}
 \frac{d\phi_2}{dT_0} = & \frac{1}{H_2} (N_{41} R_1^4 + N_{42} R_2^4 + N_{43} R_1^2 R_2^2 \\
 & + N_{44} R_1^2 + N_{45} R_2^2 + N_{46}(\epsilon \Delta) + N_{47}(\epsilon \delta)). \tag{36d}
 \end{aligned}$$

The expressions for the coefficients in Eqs. (36) are provided in Appendix C. We observe that the amplitude equations (Eqs. (36a) and (36b)) and the phase equations (Eqs. (36c) and (36d)) are decoupled. Accord-

ingly, the fixed points can be found using only the amplitude equations.

For simplicity, we first consider $\hat{\alpha}_5 = 0$, in which case the quintic amplitude equations (Eqs. (36a) and (36b)) reduce to cubic equations. It will be shown later that the nature of the fixed points thus obtained do not change even when $\hat{\alpha}_5$ is nonzero (though additional fixed points appear).

5.1 Slow-flow equations without quintic nonlinearity ($\hat{\alpha}_5 = 0$)

Setting $\hat{\alpha}_5 = 0$ in Eqs. (36a) and (36b) yields

$$\frac{dR_1}{dt} = R_1(1.7539R_1^2 + 3.1029R_2^2 + 1.0952(\epsilon\Delta) + 0.0521(\epsilon\delta)), \tag{37a}$$

$$\frac{dR_2}{dt} = R_2(-2.7897R_1^2 - 1.9717R_2^2 - 3.1200(\epsilon\Delta) + 0.0363(\epsilon\delta)). \tag{37b}$$

The fixed points of Eqs. (37) can be grouped into the following four categories:

1. Zero equilibrium solution:

$$R_1^* = 0, \quad R_2^* = 0. \tag{38}$$

2. Hopf bifurcation solution with frequency ω_1 :

$$R_1^* = \pm\sqrt{-0.6244(\epsilon\Delta) - 0.0297(\epsilon\delta)}, \tag{39a}$$

$$R_2^* = 0. \tag{39b}$$

R_1^* must be a real number, hence

$$\epsilon\delta \leq -21.0022(\epsilon\Delta). \tag{40}$$

3. Hopf bifurcation solution with frequency ω_2 :

$$R_1^* = 0, \tag{41a}$$

$$R_2^* = \pm\sqrt{-1.5824(\epsilon\Delta) + 0.0184(\epsilon\delta)}. \tag{41b}$$

Because R_2^* is real, we have the following inequality:

$$\epsilon\delta \geq 85.8457(\epsilon\Delta). \tag{42}$$

4. Quasi-periodic solution with both frequencies ω_1 and ω_2 :

$$R_1^* = \pm\sqrt{-1.4470(\epsilon\Delta) + 0.0415(\epsilon\delta)}, \tag{43a}$$

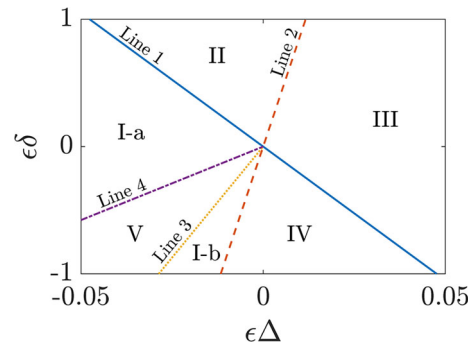


Fig. 5 Boundaries delineating six topologically distinct stability structures in $\epsilon\Delta$ and $\epsilon\delta$ parameter space. Note that $\epsilon\Delta$ and $\epsilon\delta$ denote small perturbations in τ_{cr} and k_{cr} ; hence, the origin corresponds to (τ_{cr}, k_{cr})

$$R_2^* = \pm\sqrt{0.4649(\epsilon\Delta) - 0.0402(\epsilon\delta)}. \tag{43b}$$

Because R_1^* and R_2^* are real, we have

$$\epsilon\delta \geq 34.8890(\epsilon\Delta), \tag{44a}$$

$$\epsilon\delta \leq 11.5517(\epsilon\Delta). \tag{44b}$$

Lines 1, 2, 3, and 4 in Fig. 5 are obtained using the inequality conditions of Eqs. (40), (42), (44a), and (44b), respectively. These four lines divide the parameter space of $\epsilon\Delta$ and $\epsilon\delta$ into six exclusive regions, which we denote as I-a, II, III, IV, I-b, and V. Regions I-a and I-b satisfy Eqs. (40) and (42). Region II satisfies Eq. (42). Region IV satisfies Eq. (40). Region V satisfies Eqs. (40), (42), and (44). The remaining area is Region III. Note that $\epsilon\Delta$ and $\epsilon\delta$ denote small perturbations in the delay and proportional gain parameters, respectively; hence, the origin in Fig. 5 corresponds to (τ_{cr}, k_{cr}) .

For the purpose of demonstration, we choose a representative $(\epsilon\Delta, \epsilon\delta)$ point in each region and find the fixed points R_1^* and R_2^* corresponding to it. To comment on the nature of these fixed points, we evaluate the eigenvalues ξ_1 and ξ_2 of the Jacobian matrix at these points. (This is done by taking the partial derivatives of the right-hand sides of Eqs. (37a) and (37b) with respect to R_1 and R_2 .) This analysis is presented in Table 2. We use the variables $\Gamma_0^0, \Gamma_0^{R_1}, \Gamma_{R_2}^0$, and $\Gamma_{R_2}^{R_1}$ to represent, respectively, the zero equilibrium, a Hopf bifurcation limit cycle with frequency ω_1 , a Hopf bifurcation limit cycle with frequency ω_2 , and a quasi-periodic solution. We observe from Table 2 that, depending on the value of $(\epsilon\Delta, \epsilon\delta)$, we obtain saddle points, stable

Table 2 Fixed points (R_1^* and R_2^*) and the eigenvalues of the corresponding Jacobian matrices (ξ_1 and ξ_2) in each region (I-a to V) without quintic nonlinearity. The labels $\Gamma_0^0, \Gamma_0^{R_1}, \Gamma_{R_2}^0$, and

$\Gamma_{R_2}^{R_1}$ represent, respectively, the zero equilibrium, a Hopf bifurcation limit cycle with frequency ω_1 , a Hopf bifurcation limit cycle with frequency ω_2 , and a quasi-periodic solution

Label	R_1^*	R_2^*	ξ_1	ξ_2	Nature
Region I-a ($\epsilon \Delta = -0.02, \epsilon \delta = 0$)					
Γ_0^0	0	0	0.0624	-0.0219	Saddle
$\Gamma_0^{R_1}$	± 0.1117	0	0.0438	0.0275	Unstable node
$\Gamma_{R_2}^0$	0	± 0.1779	0.0763	-0.1248	Saddle
Region II ($\epsilon \Delta = -0.005, \epsilon \delta = 0.5$)					
Γ_0^0	0	0	0.0338	0.0206	Unstable node
$\Gamma_{R_2}^0$	0	± 0.1309	0.0737	-0.0675	Saddle
Region III ($\epsilon \Delta = 0.02, \epsilon \delta = 0$)					
Γ_0^0	0	0	0.0219	-0.0624	Saddle
Region IV ($\epsilon \Delta = 0.005, \epsilon \delta = -0.5$)					
Γ_0^0	0	0	-0.0206	-0.0338	Stable node
$\Gamma_0^{R_1}$	± 0.1084	0	0.0412	-0.0665	Saddle
Region I-b ($\epsilon \Delta = -0.01, \epsilon \delta = -0.5$)					
Γ_0^0	0	0	0.0130	-0.0370	Saddle
$\Gamma_0^{R_1}$	± 0.1450	0	0.0740	-0.0459	Saddle
$\Gamma_{R_2}^0$	0	± 0.0813	-0.0165	-0.0260	Stable node
Region V ($\epsilon \Delta = -0.025, \epsilon \delta = -0.5$)					
Γ_0^0	0	0	0.0598	-0.0534	Saddle
$\Gamma_0^{R_1}$	± 0.1746	0	0.1069	-0.0252	Saddle
$\Gamma_{R_2}^0$	0	± 0.1742	0.0407	-0.1197	Saddle
$\Gamma_{R_2}^{R_1}$	± 0.1242	± 0.0922	$0.0103 + 0.0512j$	$0.0103 - 0.0512j$	Unstable focus

nodes, unstable nodes, and unstable foci. We also see that Regions I-a and I-b have fixed points of the same type: $\Gamma_0^0, \Gamma_0^{R_1}$, and $\Gamma_{R_2}^0$; however, they exhibit topologically different phase portraits. Finally, we note that Region V has unstable foci.

Although we have presented the results for stability analysis in Table 2 for only one representative point in each region, we have verified numerically that the nature of stability remains the same in a given region. For instance, we will obtain unstable foci for all parameter values belonging to Region V.

We now comment on the implications of the above analysis on a ship's roll stability for the chosen values of ($\epsilon \Delta, \epsilon \delta$). Recall that fixed points of the slow-flow amplitude equations (Eqs. (37a) and (37b)) correspond to the magnitude of the roll angle. Accordingly, the zero-amplitude fixed point (Γ_0^0) corresponds to the zero equilibrium of the ship, whereas nonzero fixed points

($\Gamma_0^{R_1}, \Gamma_{R_2}^0$, and $\Gamma_{R_2}^{R_1}$) correspond to an oscillating ship. Stable nodes are found only in Regions IV (a stable zero equilibrium) and I-b (a stable limit cycle with frequency ω_2). Because the zero equilibrium is stable in Region IV, delayed proportional control can be employed in its vicinity to maintain stability. In Region I-b, the amplitude of the stable limit cycle is 0.0813 rad, which is well below the capsizing roll angle of 0.48 rad [20], indicating the suitability of employing delayed proportional control in this region as well.

In Fig. 6, we plot the phase portraits corresponding to Eqs. (37a) and (37b) for the six regions discussed above. The phase portraits are obtained by solving Eqs. (37a) and (37b) using the ode45 ODE solver in MATLAB®. Note that the nature of each fixed point shown in Fig. 6 is indicated in the last column of Table 2.

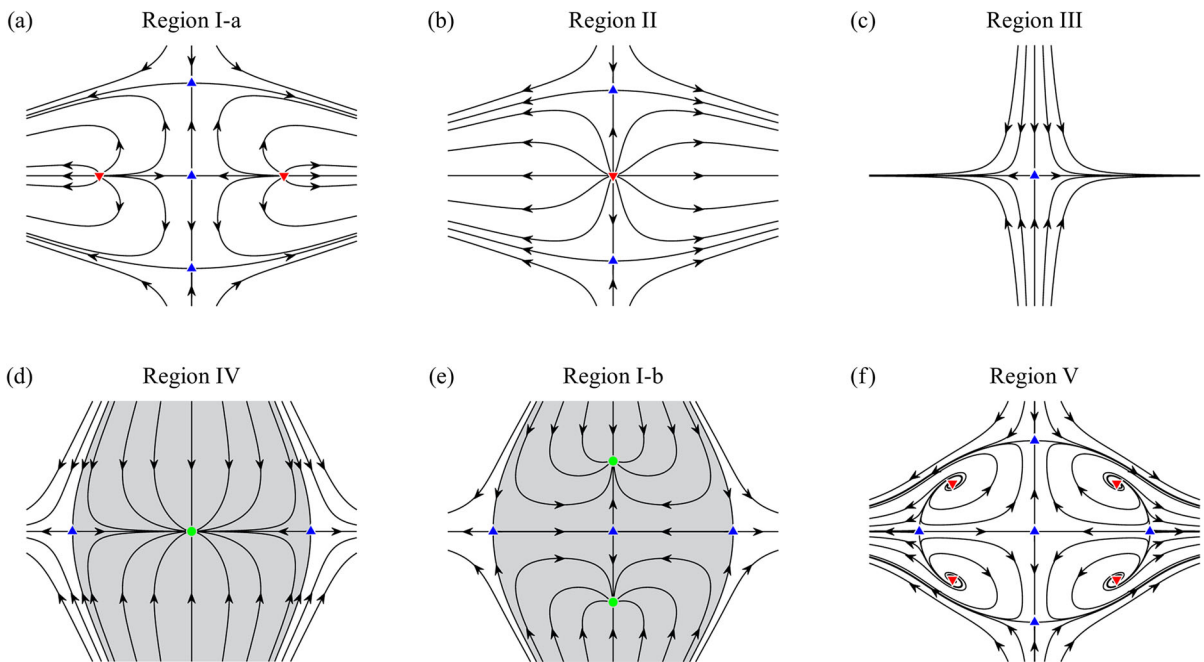


Fig. 6 Phase portraits in the six regions without the quintic nonlinearity (i.e., $\hat{\alpha}_5 = 0$) for the chosen values of $(\epsilon\Delta, \epsilon\delta)$: **a** Region I-a, **b** Region II, **c** Region III, **d** Region IV, **e** Region I-b, and **f** Region V. In each phase portrait, the horizontal axis represents R_1 , the vertical axis represents R_2 , and the origin rep-

resents the zero equilibrium. Stable nodes are shown as green circles, saddle nodes as blue upward-pointing triangles, and unstable nodes and unstable foci as red downward-pointing triangles. Shaded regions indicate basins of attraction for stable fixed points

5.2 Slow-flow equations with quintic nonlinearity

As mentioned in Sect. 5.1, setting $\hat{\alpha}_5 = 0$ in Eqs. (36) simplifies the task of finding fixed points. Using the insight from Sect. 5.1, we now investigate the more general case where $\hat{\alpha}_5 \neq 0$. For this case, the slow-flow equations are

$$\begin{aligned} \dot{R}_1 = & R_1(-0.5669R_1^4 - 1.7008R_2^4 - 3.4015R_1^2R_2^2 \\ & + 1.7539R_1^2 + 3.1029R_2^2 + 1.0952(\epsilon\Delta) \\ & + 0.0521(\epsilon\delta)), \end{aligned} \tag{45a}$$

$$\begin{aligned} \dot{R}_2 = & R_2(1.1350R_1^4 + 0.3783R_2^4 + 2.2700R_1^2R_2^2 \\ & - 2.7897R_1^2 - 1.9717R_2^2 - 3.1200(\epsilon\Delta) \\ & + 0.0363(\epsilon\delta)), \end{aligned} \tag{45b}$$

$$\begin{aligned} \dot{\phi}_1 = & 0.2457R_1^4 + 0.7371R_2^4 + 1.4743R_1^2R_2^2 \\ & - 0.9350R_1^2 - 2.8040R_2^2 - 0.5088(\epsilon\Delta) \\ & - 0.0206(\epsilon\delta), \end{aligned} \tag{45c}$$

$$\dot{\phi}_2 = 1.0285R_1^4 + 0.3428R_2^4 + 2.0570R_1^2R_2^2$$

$$\begin{aligned} & - 1.7971R_1^2 - 0.2600R_2^2 - 2.7552(\epsilon\Delta) \\ & + 0.0287(\epsilon\delta). \end{aligned} \tag{45d}$$

The right-hand sides in the amplitude equations (Eqs. (45a) and (45b)) are fifth-order polynomials; thus, we will obtain more fixed points than in Sect. 5.1. Numerical calculations reveal that the fifth-order terms have small numerical values; hence, we obtain fixed points that are numerically close to those obtained when $\hat{\alpha}_5 = 0$. Below, we will show that the stability nature of these fixed points remains the same. We focus our analysis on the new fixed points that appear when $\hat{\alpha}_5 \neq 0$.

In each region, fixed points numerically close to those listed in Table 2 were obtained and the stability nature of each of these points was the same as before. We also obtained exactly three additional fixed points in each region ($\hat{\Gamma}_0^{R_1}$, $\hat{\Gamma}_{R_2}^0$, and $\hat{\Gamma}_{R_2}^{R_1}$) having the same stability nature in each region. We use Region I-a to demonstrate our results. All the fixed points obtained in this region and the eigenvalues of the corresponding Jacobian matrices are listed in Table 3. The first three

Table 3 Fixed points (R_1^* and R_2^*) and the eigenvalues of the corresponding Jacobian matrices (ξ_1 and ξ_2) in Region I-a with quintic nonlinearity. The labels $\Gamma_0^0, \Gamma_0^{R_1}$ (or $\widehat{\Gamma}_0^{R_1}$), $\Gamma_{R_2}^0$ (or $\widehat{\Gamma}_{R_2}^0$),

and $\Gamma_{R_2}^{R_1}$ (or $\widehat{\Gamma}_{R_2}^{R_1}$) represent, respectively, the zero equilibrium, a Hopf bifurcation limit cycle with frequency ω_1 , a Hopf bifurcation limit cycle with frequency ω_2 , and a quasi-periodic solution

Label	R_1^*	R_2^*	ξ_1	ξ_2	Nature
Γ_0^0	0	0	0.0624	-0.0219	Saddle
$\Gamma_0^{R_1}$	± 0.1120	0	0.0436	0.0276	Unstable node
$\Gamma_{R_2}^0$	0	± 0.1784	0.0752	-0.1240	Saddle
$\widehat{\Gamma}_0^{R_1}$	± 1.7553	0	2.2421	-10.7201	Saddle
$\widehat{\Gamma}_{R_2}^0$	0	± 2.2759	20.1757	-29.5785	Saddle
$\widehat{\Gamma}_{R_2}^{R_1}$	± 1.4576	± 0.5016	$-2.4447 + 3.4537j$	$-2.4447 - 3.4537j$	Stable focus

fixed points ($\Gamma_0^0, \Gamma_0^{R_1}$, and $\Gamma_{R_2}^0$) are numerically close to those listed in Table 2 for Region I-a and have the same stability nature. The last three fixed points ($\widehat{\Gamma}_0^{R_1}, \widehat{\Gamma}_{R_2}^0$, and $\widehat{\Gamma}_{R_2}^{R_1}$) are the additional fixed points found when $\hat{\alpha}_5 \neq 0$.

Analysis of these results produces the following observations. In Region IV, there exist fixed points corresponding to a stable zero equilibrium and large-amplitude stable limit cycles. In Region I-b, fixed points corresponding to both small-amplitude and large-amplitude stable limit cycles exist. In all other regions, fixed points with only large-amplitude stable limit cycles exist. These phenomena are clearly illustrated in Fig. 7, which shows the phase portraits corresponding to each region. Because the trajectories are densely clustered near the origin, a magnified view near the origin is also shown for each phase portrait.

The existence of fixed points of different stability nature gives rise to interesting characteristics of ship rolling dynamics. For example, in Region IV (Fig. 7d), if the amplitude of the initial disturbance corresponds to the shaded region, then the ship stabilizes at the zero equilibrium; otherwise, it stabilizes at the large-amplitude limit cycle corresponding to $\widehat{\Gamma}_{R_2}^{R_1}$. Similarly, in Region I-b (Fig. 7e), if the amplitude of the initial disturbance corresponds to the shaded region, then the ship stabilizes at the small-amplitude limit cycle corresponding to $\Gamma_{R_2}^0$ near the origin; otherwise, it stabilizes at the large-amplitude limit cycle corresponding to $\widehat{\Gamma}_{R_2}^{R_1}$. However, we have noted in an additional analysis (not presented here) that the amplitudes of the large-amplitude limit cycles corresponding to $\widehat{\Gamma}_{R_2}^{R_1}$ are greater than the critical roll angle in all regions. For example, the amplitude of the large-amplitude limit

cycle corresponding to $\widehat{\Gamma}_{R_2}^{R_1}$ in Region I-a (see Table 3) is 1.5415 rad, which is greater than the critical roll angle of 0.48 rad. Practically, this means that the ship will capsize in all regions at the large-amplitude limit cycles corresponding to $\widehat{\Gamma}_{R_2}^{R_1}$.

6 Numerical validation of observations in Sect. 5

In Sect. 5, we used the MMS method to analyze the behavior of the system near the double Hopf bifurcation point. We observed that the $(\epsilon \Delta, \epsilon \delta)$ parametric space comprised six distinct regions of different dynamical behavior. However, MMS is an approximate numerical method; hence, it is imperative to validate the observations that were made in Sect. 5. To this end, we use direct numerical computation of the solutions of the governing differential equation (Eq. (27)). If the MMS analysis is correct, then the numerical simulations of the system should converge to the stable zero equilibrium or a stable limit cycle, as the case may be, as predicted by the MMS analysis.

The numerical simulations are performed using the `dde23` DDE solver in MATLAB[®]. The history functions $r(s)$ and $\dot{r}(s)$ for $s \in [-\tau, 0)$ used for the computations are motivated from Eq. (35) and are taken to be

$$r(s) = R_1 \sin(\omega_1 s) + R_2 \sin(\omega_2 s), \tag{46a}$$

$$\dot{r}(s) = R_1 \omega_1 \cos(\omega_1 s) + R_2 \omega_2 \cos(\omega_2 s), \tag{46b}$$

where R_1 and R_2 are constants that determine the initial point in the phase portrait. We study the effect of different initial conditions on subsequent system dynamics

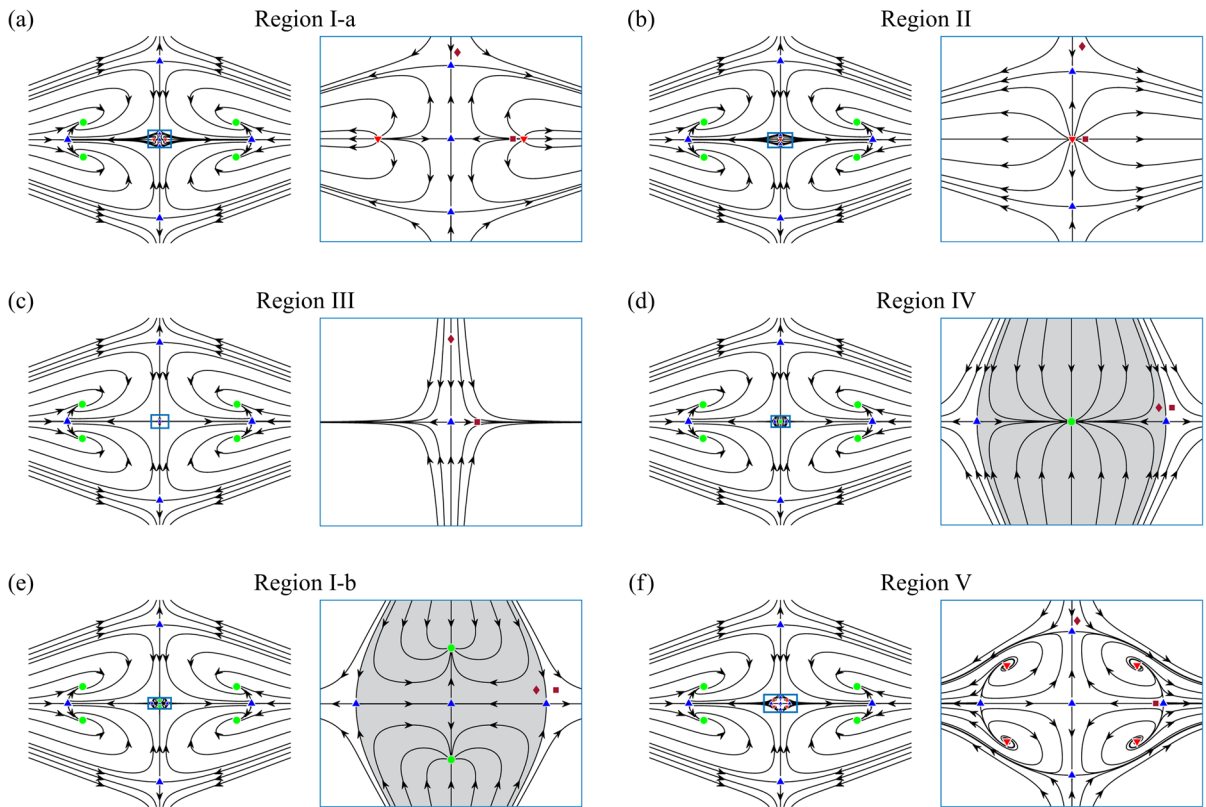


Fig. 7 Phase portraits in the six regions with the quintic nonlinearity (i.e., $\hat{\alpha}_5 \neq 0$) for the chosen values of $(\epsilon \Delta, \epsilon \delta)$: **a** Region I-a, **b** Region II, **c** Region III, **d** Region IV, **e** Region I-b, and **f** Region V. In each phase portrait, the horizontal axis represents R_1 , the vertical axis represents R_2 , and the origin represents the zero equilibrium. Stable nodes and stable foci are shown as green circles, saddle nodes as blue upward-pointing triangles,

and unstable nodes and unstable foci as red downward-pointing triangles. Diamond and square markers are initial points for the direct numerical computations presented in Sect. 6. A magnified view near the origin of each phase portrait is indicated with a blue rectangle. Shaded regions indicate basins of attraction for stable fixed points

by choosing several values of R_1 and R_2 in Eqs. (46). In Table 4, we list the values of R_1 and R_2 chosen in each region.

We now present the results of the direct numerical simulations, beginning with Region I-a. We choose R_1 and R_2 such that the initial points in the phase portrait are Q_1^{Ia} (indicated with a red diamond in Fig. 7a) and Q_2^{Ia} (indicated with a red square). It can be seen that Q_1^{Ia} is near the fixed point $\Gamma_{R_2}^0$, which is a saddle node, suggesting that the trajectory of the system will migrate to the large-amplitude stable limit cycle corresponding to $\hat{\Gamma}_{R_2}^{R_1}$. The corresponding time evolution of the system is shown in Fig. 8a. The system reaches a limit cycle in approximately 50 s. In contrast, Q_2^{Ia} is located between the unstable zero equilib-

rium and the unstable limit cycle corresponding to $\Gamma_0^{R_1}$ (red square in Fig. 7a). The trajectory in the phase portrait first approaches the origin, but is repelled toward the unstable limit cycle corresponding to $\Gamma_{R_2}^0$; it is then further deflected and, subsequently, asymptotically approaches the large-amplitude stable limit cycle corresponding to $\hat{\Gamma}_{R_2}^{R_1}$. This slow approach to the limit cycle in phase space is evident in Fig. 8b, which shows the time evolution of the system. In this case, the limit cycle is reached in approximately 200 s. Note, however, that the amplitudes of these stable limit cycles exceed the critical roll angle of 0.48 rad. Thus, practically, the ship would capsize.

Similar analyses are performed for the other regions; we summarize the results here for completeness. Fig-

Table 4 Initial points used in each region for numerical computation of solutions of Eq. (27) in terms of R_1 and R_2

Label	Symbol in Fig. 7	R_1^*	R_2^*
Region I-a ($\epsilon \Delta = -0.02, \epsilon \delta = 0$)			
Q_1^{Ia}	◆	0.01	0.21
Q_2^{Ia}	■	0.08	0
Region II ($\epsilon \Delta = -0.005, \epsilon \delta = 0.5$)			
Q_1^{II}	◆	0.015	0.18
Q_2^{II}	■	0.02	0
Region III ($\epsilon \Delta = 0.02, \epsilon \delta = 0$)			
Q_1^{III}	◆	0	0.08
Q_2^{III}	■	0.02	0
Region IV ($\epsilon \Delta = 0.005, \epsilon \delta = -0.5$)			
Q_1^{IV}	◆	0.1	0.02
Q_2^{IV}	■	0.115	0.02
Region I-b ($\epsilon \Delta = -0.01, \epsilon \delta = -0.5$)			
Q_1^{Ib}	◆	0.13	0.02
Q_2^{Ib}	■	0.16	0.02
Region V ($\epsilon \Delta = -0.025, \epsilon \delta = -0.5$)			
Q_1^V	◆	0.01	0.2
Q_2^V	■	0.16	0

Fig. 8 Time response of Eq. (27) for Region I-a with initial conditions at **a** Q_1^{Ia} , i.e., $(R_1, R_2) = (0.01, 0.21)$ and **b** Q_2^{Ia} , i.e., $(R_1, R_2) = (0.08, 0)$

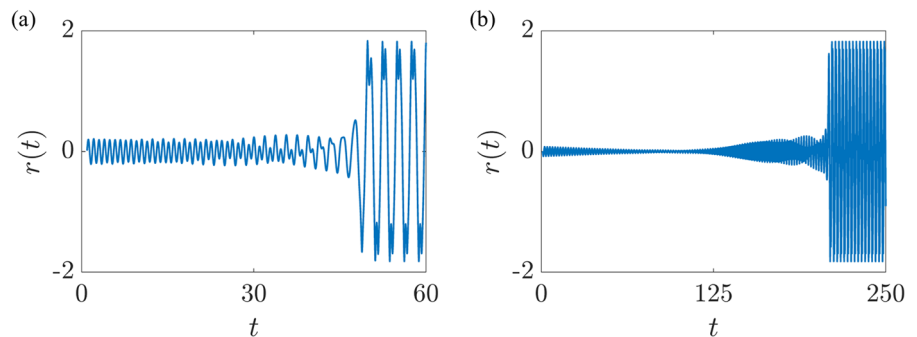


Figure 9 shows the time response of the system in Region II with initial conditions Q_1^{II} (indicated with a red diamond in Fig. 7b) and Q_2^{II} (indicated with a red square). The system reaches the large-amplitude stable limit cycle corresponding to $\widehat{\Gamma}_{R_2}^{R_1}$ in both cases. It takes longer for the system to reach the limit cycle in the case of Q_2^{II} because of the presence of an unstable limit cycle corresponding to $\Gamma_{R_2}^0$.

Figure 10 shows the time response of the system in Region III with initial conditions Q_1^{III} (indicated with a red diamond in Fig. 7c) and Q_2^{III} (indicated with a red square). The system reaches the large-amplitude stable limit cycle corresponding to $\widehat{\Gamma}_{R_2}^{R_1}$ in both cases. Fig-

ure 11 shows the time response of the system in Region IV with initial conditions Q_1^{IV} (indicated with a red diamond in Fig. 7d) and Q_2^{IV} (indicated with a red square). The system reaches the stable zero equilibrium for Q_1^{IV} and the large-amplitude stable limit cycle corresponding to $\widehat{\Gamma}_{R_2}^{R_1}$ for Q_2^{IV} .

Figure 12 shows the time response of the system in Region I-b with initial conditions Q_1^{Ib} (indicated with a red diamond in Fig. 7e) and Q_2^{Ib} (indicated with a red square). The system reaches the small-amplitude stable limit cycle corresponding to $\Gamma_{R_2}^0$ for Q_1^{Ib} and the large-amplitude stable limit cycle corresponding to $\widehat{\Gamma}_{R_2}^{R_1}$ for Q_2^{Ib} . Finally, in Fig. 13, we show the time

Fig. 9 Time response of Eq. (27) for Region II with initial conditions at **a** Q_1^{II} , i.e., $(R_1, R_2) = (0.015, 0.18)$ and **b** Q_2^{II} , i.e., $(R_1, R_2) = (0.02, 0)$

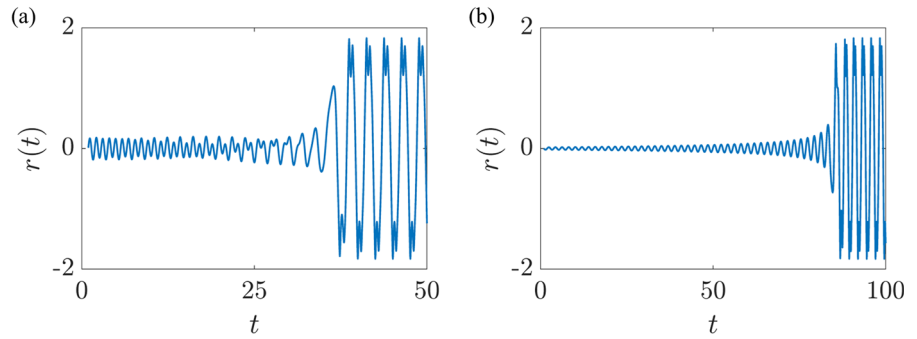


Fig. 10 Time response of Eq. (27) for Region III with initial conditions at **a** Q_1^{III} , i.e., $(R_1, R_2) = (0, 0.08)$ and **b** Q_2^{III} , i.e., $(R_1, R_2) = (0.02, 0)$

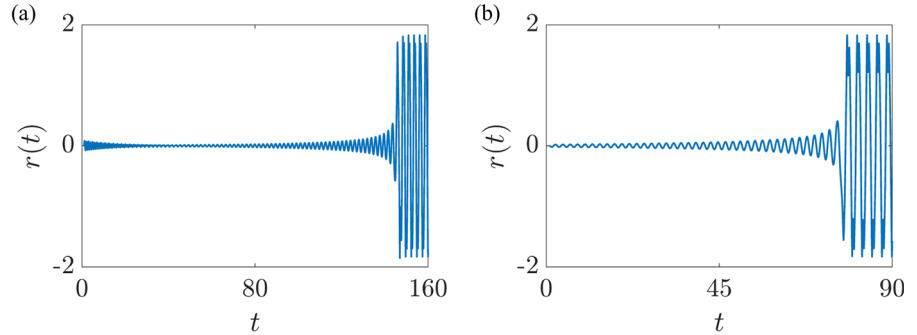
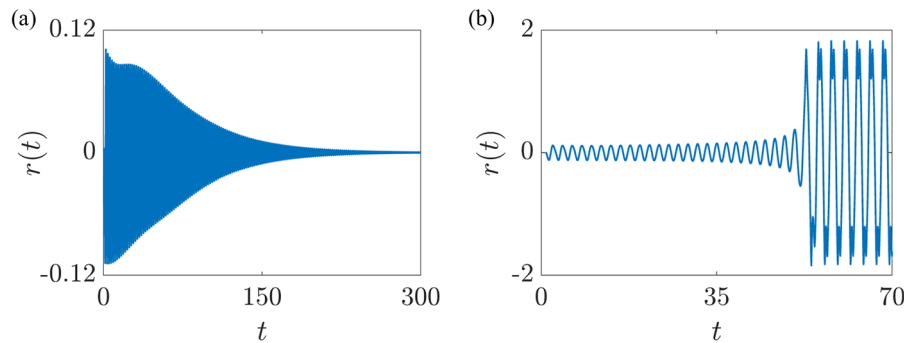


Fig. 11 Time response of Eq. (27) for Region IV with initial conditions at **a** Q_1^{IV} , i.e., $(R_1, R_2) = (0.1, 0.02)$ and **b** Q_2^{IV} , i.e., $(R_1, R_2) = (0.115, 0.02)$



response of the system in Region V with initial conditions Q_1^V (indicated with a red diamond in Fig. 7f) and Q_2^V (indicated with a red square). The system reaches the large-amplitude stable limit cycle corresponding to $\hat{\Gamma}_{R_2}^{R_1}$ in both cases. It takes longer for the system to reach the limit cycle in the case of Q_2^V because of the presence of the unstable zero equilibrium and the unstable small-amplitude limit cycle corresponding to $\Gamma_{R_2}^{R_1}$.

7 Conclusions

In this paper, we considered the roll motion of a low-freeboard ship, controlled actively with a U-tube ART with delayed feedback. The rolling dynamics of the

ship were modeled as a single-degree-of-freedom system with cubic and quintic nonlinearities. Building upon previous work in which a detailed stability analysis was performed for states near single Hopf bifurcation points, we focused this work on the first double Hopf bifurcation point. We first identified and proved the existence of the first double Hopf bifurcation point using three techniques: graphically, analytically, and through calculation of eigenvalues. We then obtained the slow-flow equations using the MMS method, bypassing the center manifold reductions and normal forms. The slow-flow equations revealed the existence of six distinct regions in the parameter space, which we labeled Regions I-a, II, III, IV, I-b, and V.

Fig. 12 Time response of Eq. (27) for Region I-b with initial conditions at **a** Q_1^{Ib} , i.e., $(R_1, R_2) = (0.13, 0.02)$ and **b** Q_2^{Ib} , i.e., $(R_1, R_2) = (0.16, 0.02)$

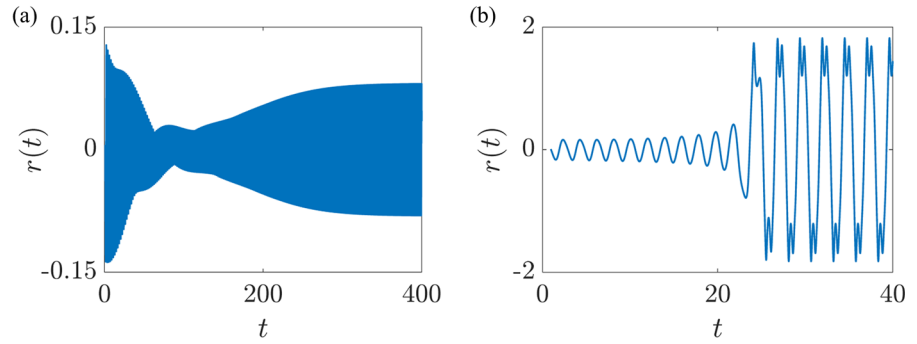
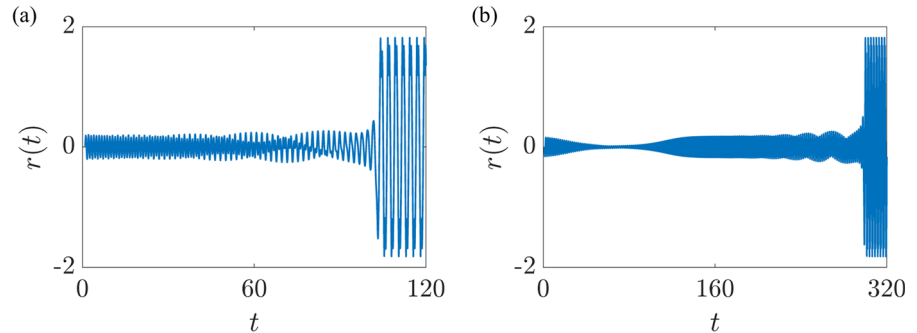


Fig. 13 Time response of Eq. (27) for Region V with initial conditions at **a** Q_1^V , i.e., $(R_1, R_2) = (0.01, 0.2)$ and **b** Q_2^V , i.e., $(R_1, R_2) = (0.16, 0)$



These regions are characterized by the nature of their fixed points and the corresponding phase portraits.

A detailed study of the fixed points in each region of the parameter space yielded interesting observations with regard to the stability of a low-freeboard ship. All six regions contain a stable large-amplitude limit cycle ($\widehat{\Gamma}_{R_2}^{R_1}$) with amplitude greater than the critical roll angle of a low-freeboard model. As a result, large disturbances will cause the ship to capsize as it evolves toward the large-amplitude limit cycle. In Regions I-a, II, III, and V, even a small disturbance could result in the capsizing of the ship due to its tendency to reach a large-amplitude limit cycle ($\widehat{\Gamma}_{R_2}^{R_1}$). In Region IV, the system has a stable zero equilibrium (Γ_0^0), so a small disturbance will subside and the ship will return to the zero equilibrium. On the other hand, in Region I-b, the system has a limit cycle ($\Gamma_{R_2}^0$) whose amplitude is less than the critical roll angle, indicating that a small disturbance will cause the ship to perform small roll oscillations without capsizing.

Based on this analysis, it can be concluded that the optimal operating region for a delayed-feedback controller is Region IV, followed by Region I-b as the second-best option. In the worst case, Regions V and I-a would provide a substantial amount of time prior to capsizing, allowing for necessary measures to be taken to

protect the crew and cargo. These qualitative observations, made from slow-flow equations, were validated through numerical simulation of the original DDE system. Future work includes experimental validation of these results and applying similar analyses to different ship models.

Author contributions All authors contributed to the conceptualization and design of the study. Mathematical modeling and numerical simulations were performed by JS. The first draft of the manuscript was written by JS. All authors contributed to the review and editing of the manuscript. All authors read and approved the final manuscript.

Funding This research received no specific support from any funding source.

Data availability Data are available from the corresponding author on reasonable request.

Declarations

Conflict of interest The authors have declared that no competing interests exist.

Appendix A: Basis functions used in Eq. (17)

The basis functions used in Eq. (17) are the shifted Legendre polynomials, which are defined as follows:

$$\Psi_1(s) = 1, \tag{A1a}$$

$$\Psi_2(s) = 1 + \frac{2s}{\tau}, \tag{A1b}$$

$$\Psi_i(s) = \frac{(2i - 3) \Psi_2(s) \Psi_{i-1}(s) - (i - 2) \Psi_{i-2}(s)}{i - 1}, \tag{A1c}$$

$$i = 3, 4, \dots$$

When these basis functions are used, the mass matrices $\mathbf{W}^{(k)}$ and stiffness matrices $\mathbf{Q}^{(k)}$ in Eq. (22) have the following simple forms:

$$W_{ij}^{(k)} = \frac{\tau}{2i - 1} \delta_{ij}, \quad i, j = 1, 2, \dots, N, \tag{A2}$$

$$Q_{ij}^{(k)} = \begin{cases} 0, & \text{if } i \geq j \\ 2, & \text{if } i < j \text{ and } i + j \text{ is odd} \\ 0, & \text{if } i < j \text{ and } i + j \text{ is even} \end{cases}, \tag{A3}$$

$$i, j = 1, 2, \dots, N.$$

Appendix B: Coefficients P_i in Eq. (32)

The coefficients P_i appearing in Eq. (32) have lengthy expressions. Thus, we provide here the expressions for only the pertinent coefficients $P_1, P_2, P_3,$ and P_4 .

$$P_1 = \frac{5}{8} \alpha_5 A_2^5 + \frac{3}{4} \alpha_3 A_2^3 + 2\omega_1 D_1 A_1 + 2\hat{\mu}_1 D_1 A_2 + 2\Delta k_{cr} \sin(\omega_1 \tau_{cr}) A_1 - 2\Delta k_{cr} \cos(\omega_1 \tau_{cr}) A_2 + \tau_{cr} k_{cr} \sin(\omega_1 \tau_{cr}) D_1 A_1 - \tau_{cr} k_{cr} \cos(\omega_1 \tau_{cr}) D_1 A_2 + \frac{3}{4} \mu_3 \omega_1^3 A_1 A_2^2 + \frac{15}{4} \alpha_5 A_2 A_3^2 A_4^2 + \frac{15}{4} \alpha_5 A_1^2 A_2 A_3^2 + \frac{15}{4} \alpha_5 A_1^2 A_2 A_4^2 + \frac{3}{2} \mu_3 \omega_1 \omega_2^2 A_1 A_2^2 + \frac{3}{2} \mu_3 \omega_1 \omega_2^2 A_1 A_4^2 + \frac{15}{4} \alpha_5 A_2^3 A_3^2 + \frac{15}{4} \alpha_5 A_2^3 A_4^2 + \frac{5}{4} \alpha_5 A_1^2 A_2^3 - \delta \sin(\omega_1 \tau_{cr}) A_1 + \delta \cos(\omega_1 \tau_{cr}) A_2 + \frac{3}{4} \alpha_3 A_1^2 A_2 + \frac{3}{2} \alpha_3 A_2 A_3^2 + \frac{3}{2} \alpha_3 A_2 A_4^2 + \frac{3}{4} \mu_3 \omega_1^3 A_1^3 + \frac{15}{8} \alpha_5 A_2 A_3^4 + \frac{5}{8} \alpha_5 A_1^4 A_2 + \frac{15}{8} \alpha_5 A_2 A_4^4 - 2\Delta \omega_0^2 A_2 - 2\Delta \hat{\mu}_1 \omega_1 A_1, \tag{B4}$$

$$P_2 = \frac{3}{4} \alpha_3 A_1^3 - 2\omega_1 D_1 A_2 + 2\hat{\mu}_1 D_1 A_1 + \frac{5}{8} \alpha_5 A_1^5 + \frac{15}{4} \alpha_5 A_1 A_3^2 A_4^2 + \frac{15}{4} \alpha_5 A_1 A_2^2 A_3^2 + \frac{15}{4} \alpha_5 A_1 A_2^2 A_4^2 - \tau_{cr} k_{cr} \cos(\omega_1 \tau_{cr}) D_1 A_1 - \tau_{cr} k_{cr} \sin(\omega_1 \tau_{cr}) D_1 A_2 - 2\Delta k_{cr} \cos(\omega_1 \tau_{cr}) A_1 - 2\Delta k_{cr} \sin(\omega_1 \tau_{cr}) A_2 - \frac{3}{4} \mu_3 \omega_1^3 A_1^2 A_2 - \frac{3}{2} \mu_3 \omega_1 \omega_2^2 A_2 A_4^2 - \frac{3}{2} \mu_3 \omega_1 \omega_2^2 A_2 A_3^2 - \frac{3}{4} \mu_3 \omega_1^3 A_2^3 + \frac{15}{8} \alpha_5 A_1 A_4^4 + \frac{5}{8} \alpha_5 A_1 A_4^2 + \frac{15}{8} \alpha_5 A_1 A_3^4 + \frac{5}{4} \alpha_5 A_1^3 A_2^2 + \frac{15}{4} \alpha_5 A_1^3 A_2^2 + \frac{15}{4} \alpha_5 A_1^3 A_3^2 + \frac{15}{4} \alpha_5 A_1^3 A_4^2 + \delta \sin(\omega_1 \tau_{cr}) A_2 + \delta \cos(\omega_1 \tau_{cr}) A_1 + \frac{3}{2} \alpha_3 A_1 A_4^2 + \frac{3}{4} \alpha_3 A_1 A_2^2 + \frac{3}{2} \alpha_3 A_1 A_3^2 - 2\Delta \omega_0^2 A_1 + 2\Delta \hat{\mu}_1 \omega_1 A_2, \tag{B5}$$

$$P_3 = \tau_{cr} k_{cr} \sin(\omega_2 \tau_{cr}) D_1 A_3 - \tau_{cr} k_{cr} \cos(\omega_2 \tau_{cr}) D_1 A_4 + 2\Delta k_{cr} \sin(\omega_2 \tau_{cr}) A_3 - 2\Delta k_{cr} \cos(\omega_2 \tau_{cr}) A_4 + \frac{3}{4} \mu_3 \omega_2^3 A_3 A_4^2 + \frac{15}{4} \alpha_5 A_1^2 A_2^2 A_4 + \frac{15}{4} \alpha_5 A_1^2 A_2^2 A_3^2 + \frac{15}{4} \alpha_5 A_2^2 A_3^2 A_4 + \frac{15}{4} \alpha_5 A_2^2 A_4^3 + \frac{15}{4} \alpha_5 A_1^2 A_4^3 + \frac{5}{4} \alpha_5 A_2^2 A_3^3 - \delta \sin(\omega_2 \tau_{cr}) A_3 + \delta \cos(\omega_2 \tau_{cr}) A_4 + \frac{3}{2} \alpha_3 A_1^2 A_4 + \frac{3}{2} \alpha_3 A_2^2 A_4 + \frac{3}{4} \alpha_3 A_3^2 A_4 + \frac{3}{4} \mu_3 \omega_2^3 A_3^3 + \frac{15}{8} \alpha_5 A_2^4 A_4 + \frac{15}{8} \alpha_5 A_1^4 A_4 + \frac{5}{8} \alpha_5 A_3^4 A_4 + \frac{5}{8} \alpha_5 A_4^5 + \frac{3}{4} \alpha_3 A_4^3 + 2\omega_2 D_1 A_3 + 2\hat{\mu}_1 D_1 A_4 + \frac{3}{2} \mu_3 \omega_1^2 \omega_2 A_1^2 A_3 + \frac{3}{2} \mu_3 \omega_1^2 \omega_2 A_2^2 A_3 - 2\Delta \hat{\mu}_1 \omega_2 A_3 - 2\Delta \omega_0^2 A_4, \tag{B6}$$

$$P_4 = \frac{5}{8} \alpha_5 A_3^5 + \frac{3}{4} \alpha_3 A_3^3 - 2\omega_2 D_1 A_4 + 2\hat{\mu}_1 D_1 A_3 + \frac{15}{4} \alpha_5 A_1^2 A_2^2 A_3 + \frac{15}{4} \alpha_5 A_1^2 A_3 A_4^2 + \frac{15}{4} \alpha_5 A_2^2 A_3 A_4^2 - 2\Delta \omega_0^2 A_3 + 2\Delta \omega_2 \hat{\mu}_1 A_4 - \tau_{cr} k_{cr} \cos(\omega_2 \tau_{cr}) D_1 A_3 - \tau_{cr} k_{cr} \sin(\omega_2 \tau_{cr}) D_1 A_4 + \frac{5}{4} \alpha_5 A_3^3 A_4^2 - \frac{3}{4} \mu_3 \omega_2^3 A_3^2 A_4 - \frac{3}{2} \mu_3 \omega_1^2 \omega_2 A_1^2 A_4 - \frac{3}{2} \mu_3 \omega_1^2 \omega_2 A_2^2 A_4 + \frac{15}{4} \alpha_5 A_2^2 A_3^3 + \frac{15}{4} \alpha_5 A_1^2 A_3^3 + \frac{3}{2} \alpha_3 A_1^2 A_3 + \frac{3}{2} \alpha_3 A_2^2 A_3 + \frac{3}{4} \alpha_3 A_3 A_4^2 - \frac{3}{4} \mu_3 \omega_2^3 A_3^4 + \frac{15}{8} \alpha_5 A_2^4 A_3 + \frac{15}{8} \alpha_5 A_1^4 A_3 + \frac{5}{8} \alpha_5 A_3 A_4^4 + \delta \sin(\omega_2 \tau_{cr}) A_4 + \delta \cos(\omega_2 \tau_{cr}) A_3$$

$$-2\Delta k_{cr} A_3 \cos(\omega_2 \tau_{cr}) - 2\Delta k_{cr} A_4 \sin(\omega_2 \tau_{cr}), \quad (B7)$$

$$\text{where } A_i = A_i(T_1) \text{ and } D_1 A_i = \frac{dA_i(T_1)}{dT_1}.$$

Appendix C: Coefficients N_i in Eqs. (36)

The expressions for the coefficients in Eqs. (36) are as follows:

$$\begin{aligned} H_1 &= 8k_{cr} \tau_{cr} (4\omega_1 \sin(\omega_1 \tau_{cr}) - 4\hat{\mu}_1 \cos(\omega_1 \tau_{cr}) \\ &\quad + k_{cr} \tau_{cr}) + 32 (\hat{\mu}_1^2 + \omega_1^2), \\ H_2 &= 8k_{cr} \tau_{cr} (4\omega_2 \sin(\omega_2 \tau_{cr}) - 4\hat{\mu}_1 \cos(\omega_2 \tau_{cr}) \\ &\quad + k_{cr} \tau_{cr}) + 32 (\hat{\mu}_1^2 + \omega_2^2), \\ N_{11} &= 5\hat{\alpha}_5 (k_{cr} \tau_{cr} \cos(\omega_1 \tau_{cr}) - 2\hat{\mu}_1), \\ N_{12} &= 15\hat{\alpha}_5 (k_{cr} \tau_{cr} \cos(\omega_1 \tau_{cr}) - 2\hat{\mu}_1), \\ N_{13} &= 30\hat{\alpha}_5 (k_{cr} \tau_{cr} \cos(\omega_1 \tau_{cr}) - 2\hat{\mu}_1), \\ N_{14} &= 6[\hat{\alpha}_3 (k_{cr} \tau_{cr} \cos(\omega_1 \tau_{cr}) - 2\hat{\mu}_1) \\ &\quad - \hat{\mu}_3 \omega_1^3 (k_{cr} \tau_{cr} \sin(\omega_1 \tau_{cr}) + 2\omega_1)], \\ N_{15} &= 12[\hat{\alpha}_3 (k_{cr} \tau_{cr} \cos(\omega_1 \tau_{cr}) - 2\hat{\mu}_1) \\ &\quad - \hat{\mu}_3 \omega_1 \omega_2^2 (k_{cr} \tau_{cr} \sin(\omega_1 \tau_{cr}) - 2\omega_1)], \\ N_{16} &= 16[2\hat{\mu}_1 (\omega_0^2 + \omega_1^2) + k_{cr} \omega_1 (\tau_{cr} \hat{\mu}_1 - 2) \\ &\quad \sin(\omega_1 \tau_{cr}) - k_{cr} (\tau_{cr} \omega_0^2 - 2\hat{\mu}_1) \cos(\omega_1 \tau_{cr}) \\ &\quad - k_{cr}^2 \tau_{cr}], \\ N_{17} &= 16 (\omega_1 \sin(\omega_1 \tau_{cr}) - \hat{\mu}_1 \cos(\omega_1 \tau_{cr})) + 8k_{cr} \tau_{cr}, \\ N_{21} &= 15\hat{\alpha}_5 (k_{cr} \tau_{cr} \cos(\omega_2 \tau_{cr}) - 2\hat{\mu}_1), \\ N_{22} &= 5\hat{\alpha}_5 (k_{cr} \tau_{cr} \cos(\omega_2 \tau_{cr}) - 2\hat{\mu}_1), \\ N_{23} &= 30\hat{\alpha}_5 (k_{cr} \tau_{cr} \cos(\omega_2 \tau_{cr}) - 2\hat{\mu}_1), \\ N_{24} &= 12[\hat{\alpha}_3 (k_{cr} \tau_{cr} \cos(\omega_2 \tau_{cr}) - 2\hat{\mu}_1) \\ &\quad - \hat{\mu}_3 \omega_1^2 \omega_2 (k_{cr} \tau_{cr} \sin(\omega_2 \tau_{cr}) + 2\omega_2)], \\ N_{25} &= 6[\hat{\alpha}_3 (k_{cr} \tau_{cr} \cos(\omega_2 \tau_{cr}) - 2\hat{\mu}_1) \\ &\quad - \hat{\mu}_3 \omega_2^3 (k_{cr} \tau_{cr} \sin(\omega_2 \tau_{cr}) + 2\omega_2)], \\ N_{26} &= 16[2\hat{\mu}_1 (\omega_0^2 + \omega_2^2) + k_{cr} \omega_2 (\tau_{cr} \hat{\mu}_1 - 2) \\ &\quad \sin(\omega_2 \tau_{cr}) - k_{cr} (\tau_{cr} \omega_0^2 - 2\hat{\mu}_1) \cos(\omega_2 \tau_{cr}) \\ &\quad - k_{cr}^2 \tau_{cr}], \\ N_{27} &= 16 (\omega_2 \sin(\omega_2 \tau_{cr}) - \hat{\mu}_1 \cos(\omega_2 \tau_{cr})) + 8k_{cr} \tau_{cr}, \\ N_{31} &= 5\hat{\alpha}_5 (k_{cr} \tau_{cr} \sin(\omega_1 \tau_{cr}) + 2\omega_1), \\ N_{32} &= 15\hat{\alpha}_5 (k_{cr} \tau_{cr} \sin(\omega_1 \tau_{cr}) + 2\omega_1), \end{aligned}$$

$$\begin{aligned} N_{33} &= 30\hat{\alpha}_5 (k_{cr} \tau_{cr} \sin(\omega_1 \tau_{cr}) + 2\omega_1), \\ N_{34} &= 6[\hat{\mu}_3 \omega_1^3 (k_{cr} \tau_{cr} \cos(\omega_1 \tau_{cr}) - 2\hat{\mu}_1) \\ &\quad + \hat{\alpha}_3 (k_{cr} \tau_{cr} \sin(\omega_1 \tau_{cr}) + 2\omega_1)], \\ N_{35} &= 12[\hat{\mu}_3 \omega_1 \omega_2^2 (k_{cr} \tau_{cr} \cos(\omega_1 \tau_{cr}) - 2\hat{\mu}_1) \\ &\quad + \hat{\alpha}_3 (k_{cr} \tau_{cr} \sin(\omega_1 \tau_{cr}) + 2\omega_1)], \\ N_{36} &= 16[\omega_1 (2\hat{\mu}_1^2 - 2\omega_0^2 - k_{cr} (2 + \tau_{cr} \hat{\mu}_1) \\ &\quad \cos(\omega_1 \tau_{cr})) - k_{cr} (2\hat{\mu}_1 + \tau_{cr} \omega_0^2) \sin(\omega_1 \tau_{cr})], \\ N_{37} &= 16 (\hat{\mu}_1 \sin(\omega_1 \tau_{cr}) + \omega_1 \cos(\omega_1 \tau_{cr})), \\ N_{41} &= 15\hat{\alpha}_5 (k_{cr} \tau_{cr} \sin(\omega_2 \tau_{cr}) + 2\omega_2), \\ N_{42} &= 5\hat{\alpha}_5 (k_{cr} \tau_{cr} \sin(\omega_2 \tau_{cr}) + 2\omega_2), \\ N_{43} &= 30\hat{\alpha}_5 (k_{cr} \tau_{cr} \sin(\omega_2 \tau_{cr}) + 2\omega_2), \\ N_{44} &= 12[\hat{\mu}_3 \omega_2 \omega_1^2 (k_{cr} \tau_{cr} \cos(\omega_2 \tau_{cr}) - 2\hat{\mu}_1) \\ &\quad + \hat{\alpha}_3 (k_{cr} \tau_{cr} \sin(\omega_2 \tau_{cr}) + 2\omega_2)], \\ N_{45} &= 6[\hat{\mu}_3 \omega_2^3 (k_{cr} \tau_{cr} \cos(\omega_2 \tau_{cr}) - 2\hat{\mu}_1) \\ &\quad + \hat{\alpha}_3 (k_{cr} \tau_{cr} \sin(\omega_2 \tau_{cr}) + 2\omega_2)], \\ N_{46} &= 16[\omega_2 (2\hat{\mu}_1^2 - 2\omega_0^2 - k_{cr} (2 + \tau_{cr} \hat{\mu}_1) \\ &\quad \cos(\omega_2 \tau_{cr})) - k_{cr} (2\hat{\mu}_1 + \tau_{cr} \omega_0^2) \sin(\omega_2 \tau_{cr})], \\ N_{47} &= 16 (\hat{\mu}_1 \sin(\omega_2 \tau_{cr}) + \omega_2 \cos(\omega_2 \tau_{cr})). \end{aligned}$$

References

- Zhou, B., Qi, X., Zhang, J., Zhang, H.: Effect of 6-DOF oscillation of ship target on SAR imaging. *Remote Sens.* **13**(9), 1821 (2021). <https://doi.org/10.3390/rs13091821>
- Holden, C.: Modeling and control of parametric roll resonance. Ph.D. thesis, Department of Engineering Cybernetics, Norwegian University of Science and Technology, Trondheim, Norway (2011). <https://hdl.handle.net/11250/260315>
- Perez, T., Blanke, M.: Ship roll damping control. *Annu. Rev. Control.* **36**(1), 129–147 (2012). <https://doi.org/10.1016/j.arcontrol.2012.03.010>
- Minorsky, N.: Problems of anti-rolling stabilization of ships by the activated tank method. *J. Am. Soc. Nav. Eng.* **47**(1), 87–119 (1935). <https://doi.org/10.1111/j.1559-3584.1935.tb04304.x>
- Marzouk, O.A., Nayfeh, A.H.: Control of ship roll using passive and active anti-roll tanks. *Ocean Eng.* **36**(9–10), 661–671 (2009). <https://doi.org/10.1016/j.oceaneng.2009.03.005>
- Nayfeh, A.H., Khdeir, A.A.: Nonlinear rolling of ships in regular beam seas. *Int. Shipbuild. Prog.* **33**(379), 40–49 (1986). <https://doi.org/10.3233/isp-1986-3337901>
- Nayfeh, A.H., Khdeir, A.A.: Nonlinear rolling of biased ships in regular beam waves. *Int. Shipbuild. Prog.* **33**(381), 84–93 (1986). <https://doi.org/10.3233/isp-1986-3338102>
- Spyrou, K.J., Thompson, J.M.T.: The nonlinear dynamics of ship motions: a field overview and some recent develop-

- ments. *Philos. Trans. A Math. Phys. Eng. Sci.* **358**(1771), 1735–1760 (2000). <https://doi.org/10.1098/rsta.2000.0613>
9. Spyrou, K.J.: Design criteria for parametric rolling. *Ocean Eng. Int.* **9**(1), 11–27 (2005)
 10. Ibrahim, R.A., Grace, I.M.: Modeling of ship roll dynamics and its coupling with heave and pitch. *Math. Probl. Eng.* **2010**, 934714 (2010). <https://doi.org/10.1155/2010/934714>
 11. Neves, M.A.S.: Dynamic stability of ships in regular and irregular seas - an overview. *Ocean Eng.* **120**, 362–370 (2016). <https://doi.org/10.1016/j.oceaneng.2016.02.010>
 12. Vugts, J.H.: A comparative study on four different passive roll damping tanks. *Int. Shipbuild. Prog.* **16**(179), 212–223 (1969). <https://doi.org/10.3233/isp-1969-1617903>
 13. Shin, Y.S., Belenky, V.L., Lin, W.M., Weems, K.M., Engle, A.H.: Nonlinear time domain simulation technology for sea-keeping and wave-load analysis for modern ship design. *Trans. Soc. Nav. Archit. Mar. Eng.* **111**, 557–583 (2003)
 14. Phairoh, T., Huang, J.K.: Modeling and analysis of ship roll tank stimulator systems. *Ocean Eng.* **32**(8–9), 1037–1053 (2005). <https://doi.org/10.1016/j.oceaneng.2004.09.007>
 15. Alujević, N., Čatipović, I., Malenica, Š., Senjanović, I., Vladimir, N.: Ship roll control and power absorption using a U-tube anti-roll tank. *Ocean Eng.* **172**, 857–870 (2019). <https://doi.org/10.1016/j.oceaneng.2018.12.007>
 16. Abdel Gawad, A.F., Ragab, S.A., Nayfeh, A.H., Mook, D.T.: Roll stabilization by anti-roll passive tanks. *Ocean Eng.* **28**(5), 457–469 (2001). [https://doi.org/10.1016/S0029-8018\(00\)00015-9](https://doi.org/10.1016/S0029-8018(00)00015-9)
 17. Moaleji, R., Greig, A.R.: On the development of ship anti-roll tanks. *Ocean Eng.* **34**(1), 103–121 (2007). <https://doi.org/10.1016/j.oceaneng.2005.12.013>
 18. Kučera, V., Pilbauer, D., Vyhřídál, T., Olgac, N.: Extended delayed resonators - design and experimental verification. *Mechatronics* **41**, 29–44 (2017). <https://doi.org/10.1016/j.mechatronics.2016.10.019>
 19. Spyrou, K.J.: On course-stability and control delay. *Int. Shipbuild. Prog.* **46**(448), 421–443 (1999)
 20. Shaik, J., Uchida, T.K., Vyasarayani, C.P.: Effect of delay on control of direct resonance of ships in beam waves using a proportional-derivative controller with delay. *J. Comput. Nonlinear Dyn.* **17**(6), 061004 (2022). <https://doi.org/10.1115/1.4053561>
 21. Yu, P.: Analysis on double Hopf bifurcation using computer algebra with the aid of multiple scales. *Nonlinear Dyn.* **27**(1), 19–53 (2002). <https://doi.org/10.1023/a:1017993026651>
 22. Moroz, I.M., Brindley, J.: An example of two-mode interaction in a three-layer model of baroclinic instability. *Phys. Lett. A* **91**(5), 226–230 (1982). [https://doi.org/10.1016/0375-9601\(82\)90477-7](https://doi.org/10.1016/0375-9601(82)90477-7)
 23. Cox, S.M., Leibovich, S., Moroz, I.M., Tandon, A.: Hopf bifurcations in Langmuir circulations. *Physica D* **59**(1–3), 226–254 (1992). [https://doi.org/10.1016/0167-2789\(92\)90217-b](https://doi.org/10.1016/0167-2789(92)90217-b)
 24. Lewis, G.M., Nagata, W.: Double Hopf bifurcations in the differentially heated rotating annulus. *SIAM J. Appl. Math.* **63**(3), 1029–1055 (2003). <https://doi.org/10.1137/s0036139901386405>
 25. Marques, F., Lopez, J.M., Shen, J.: Mode interactions in an enclosed swirling flow: a double Hopf bifurcation between azimuthal wavenumbers 0 and 2. *J. Fluid Mech.* **455**, 263–281 (2002). <https://doi.org/10.1017/s0022112001007285>
 26. Kalmár-Nagy, T., Stépán, G., Moon, F.C.: Subcritical Hopf bifurcation in the delay equation model for machine tool vibrations. *Nonlinear Dyn.* **26**(2), 121–142 (2001). <https://doi.org/10.1023/a:1012990608060>
 27. Wang, Z., Hu, H.: Dimensional reduction for nonlinear time-delayed systems composed of stiff and soft substructures. *Nonlinear Dyn.* **25**(4), 317–331 (2001). <https://doi.org/10.1023/a:1012981822882>
 28. Fofana, M.S.: Delay dynamical systems and applications to nonlinear machine-tool chatter. *Chaos, Solitons Fractals* **17**(4), 731–747 (2003). [https://doi.org/10.1016/s0960-0779\(02\)00407-1](https://doi.org/10.1016/s0960-0779(02)00407-1)
 29. Molnar, T.G., Dombóvari, Z., Insuperger, T., Stepan, G.: On the analysis of the double Hopf bifurcation in machining processes via centre manifold reduction. *Proc. R. Soc. A Math. Phys. Eng. Sci.* **473**(2207), 20170502 (2017). <https://doi.org/10.1098/rspa.2017.0502>
 30. Faria, T., Magalhães, L.T.: Normal forms for retarded functional differential equations and applications to Bogdanov-Takens singularity. *J. Differ. Equ.* **122**(2), 201–224 (1995). <https://doi.org/10.1006/jdeq.1995.1145>
 31. Faria, T., Magalhães, L.T.: Normal forms for retarded functional differential equations with parameters and applications to Hopf bifurcation. *J. Differ. Equ.* **122**(2), 181–200 (1995). <https://doi.org/10.1006/jdeq.1995.1144>
 32. Faria, T.: Normal forms for periodic retarded functional differential equations. *Proc. R. Soc. Edinb. A Math.* **127**(1), 21–46 (1997). <https://doi.org/10.1017/s0308210500023490>
 33. Stépán, G., Haller, G.: Quasiperiodic oscillations in robot dynamics. *Nonlinear Dyn.* **8**(4), 513–528 (1995). <https://doi.org/10.1007/bf00045711>
 34. Nayfeh, A.H., Chin, C.M., Pratt, J.: In *Dynamics and Chaos*. In: Moon, F.C. (ed.) *Manufacturing Processes*, pp. 193–213. Wiley, New York, NY, USA (1997)
 35. Das, S.L., Chatterjee, A.: Multiple scales without center manifold reductions for delay differential equations near Hopf bifurcations. *Nonlinear Dyn.* **30**(4), 323–335 (2002). <https://doi.org/10.1023/a:1021220117746>
 36. Wahi, P., Chatterjee, A.: Regenerative tool chatter near a codimension 2 Hopf point using multiple scales. *Nonlinear Dyn.* **40**(4), 323–338 (2005). <https://doi.org/10.1007/s11071-005-7292-9>
 37. Dalzell, J.F.: A note on the form of ship roll damping. *J. Ship Res.* **22**(3), 178–185 (1978). <https://doi.org/10.5957/jsr.1978.22.3.178>
 38. Wright, J.H.G., Marshfield, W.B.: Ship roll response and capsize behaviour in beam seas. *Trans. R. Inst. Nav. Archit.* **122**, 129–148 (1980)
 39. Kuznetsov, Y.A.: *Elements of Applied Bifurcation Theory*, 3rd edn. Springer-Verlag, New York, NY, USA (2004). <https://doi.org/10.1007/978-1-4757-3978-7>
 40. Nayfeh, A.H., Balachandran, B.: *Applied Nonlinear Dynamics: Analytical, Computational, and Experimental Methods*. Wiley-VCH, Weinheim, Germany (2004)
 41. Pei, L., Wang, S.: Double Hopf bifurcation of differential equation with linearly state-dependent delays via MMS. *Appl. Math. Comput.* **341**, 256–276 (2019). <https://doi.org/10.1016/j.amc.2018.08.040>
 42. Vyasarayani, C.P., Subhash, S., Kalmár-Nagy, T.: Spectral approximations for characteristic roots of delay differential

- equations. *Int. J. Dyn. Control* **2**(2), 126–132 (2014). <https://doi.org/10.1007/s40435-014-0060-2>
43. Stépán, G., Kalmar-Nagy, T.: Nonlinear regenerative machine tool vibrations. In *Proceedings of the ASME 1997 Design Engineering Technical Conferences. Volume 1C: 16th Biennial Conference on Mechanical Vibration and Noise* (Sacramento, CA, USA, 1997), p. V01CT12A008. <https://doi.org/10.1115/detc97/vib-4021>
44. Stépán, G.: Modelling nonlinear regenerative effects in metal cutting. *Philos. Trans. A Math. Phys. Eng. Sci.* **359**(1781), 739–757 (2001). <https://doi.org/10.1098/rsta.2000.0753>

Publisher's Note Springer Nature remains neutral with regard to jurisdictional claims in published maps and institutional affiliations.

Springer Nature or its licensor (e.g. a society or other partner) holds exclusive rights to this article under a publishing agreement with the author(s) or other rightsholder(s); author self-archiving of the accepted manuscript version of this article is solely governed by the terms of such publishing agreement and applicable law.